NeuroImage 202 (2019) 116031

Contents lists available at ScienceDirect

NeuroImage

journal homepage: www.elsevier.com/locate/neuroimage

Bifurcation structure determines different phase-amplitude coupling patterns in the activity of biologically plausible neural networks

Osvaldo Matías Velarde, Eugenio Urdapilleta, Germán Mato **, Damián Dellavale *

Centro Atómico Bariloche and Instituto Balseiro, Comisión Nacional de Energía Atómica (CNEA), Consejo Nacional de Investigaciones Científicas y Técnicas (CONICET), Universidad Nacional de Cuyo (UNCUYO), Av. E. Bustillo 9500, R8402AGP, San Carlos de Bariloche, Río Negro, Argentina

ARTICLE INFO

Keywords:
Cross-frequency coupling
Phase-amplitude coupling
Bifurcation structure
Neural network
Parkinson's disease

ABSTRACT

Phase-amplitude cross frequency coupling (PAC) is a rather ubiquitous phenomenon that has been observed in a variety of physical domains; however, the mechanisms underlying the emergence of PAC and its functional significance in the context of neural processes are open issues under debate.

In this work we analytically demonstrate that PAC phenomenon naturally emerges in mean-field models of biologically plausible networks, as a signature of specific bifurcation structures. The proposed analysis, based on bifurcation theory, allows the identification of the mechanisms underlying oscillatory dynamics that are essentially different in the context of PAC. Specifically, we found that two PAC classes can coexist in the complex dynamics of the analyzed networks: 1) harmonic PAC which is an epiphenomenon of the nonsinusoidal waveform shape characterized by the linear superposition of harmonically related spectral components, and 2) nonharmonic PAC associated with "true" coupled oscillatory dynamics with independent frequencies elicited by a secondary Hopf bifurcation and mechanisms involving periodic excitation/inhibition (PEI) of a network population. Importantly, these two PAC types have been experimentally observed in a variety of neural architectures confounding traditional parametric and nonparametric PAC metrics, like those based on linear filtering or the waveform shape analysis, due to the fact that these methods operate on a single one-dimensional projection of an intrinsically multidimensional system dynamics.

We exploit the proposed tools to study the functional significance of the PAC phenomenon in the context of Parkinson's disease (PD). Our results show that pathological slow oscillations (e.g. β band) and nonharmonic PAC patterns emerge from dissimilar underlying mechanisms (bifurcations) and are associated to the competition of different BG-thalamocortical loops. Thus, this study provides theoretical arguments that demonstrate that nonharmonic PAC is not an epiphenomenon related to the pathological β band oscillations, thus supporting the experimental evidence about the relevance of PAC as a potential biomarker of PD.

1. Introduction

Cross-Frequency Coupling (CFC) is a useful conceptualization regarding signal analysis, in which certain characteristics (e.g. amplitude, phase) of a frequency band govern or interact with others in a different band, either in the same signal or in another related one. This general phenomenon has been observed in a variety of time series across very different disciplines, ranging from nonlinear acoustics related to externally modulated bubble dynamics (Dellavale and Rossell, 2019), to physiological signals in the endocrine (Walker et al., 2010; Dietrich et al., 2012; Hoermann et al., 2015) or in the vascular systems (Ieva et al., 2013), dynamic processes with bridge-vehicle interaction (Yang and Lin, 2005), the complex nonlinear coupling between atmospheric variables (Laskar et al., 2014; Eswaraiah et al., 2018; Paluš, 2014), and the number of sunspots, or related measures, determined from astronomical observations (Hathaway, 2010; Shapoval et al., 2017), among others. In recent years, different kinds of CFC analysis have received much attention in neuroscience, probably boosted by the richness in frequency content of brain signals, the tight association between cognitive or perceptual processes to specific frequency bands in different types of electrophysiological signals, and more importantly, because these interactions between brain oscillations have been hypothesized to have important

* Corresponding author.
** Corresponding author.
E-mail addresses: matog@cab.cnea.gov.ar (G. Mato), dellavale@cab.cnea.gov.ar (D. Dellavale).

https://doi.org/10.1016/j.neuroimage.2019.116031
Received 22 March 2019; Received in revised form 10 July 2019; Accepted 16 July 2019
Available online 19 July 2019

functional roles (Fries, 2005; Jensen and Colgin, 2007; Canolty and Knight, 2010; Hyafil et al., 2015b). In this regard, CFC processes have been observed in brain activity across species, including humans, in connection with various physiological (Bragin et al., 1995; Lakatos et al., 2005, 2008; Palva et al., 2005; Canolty et al., 2006; Tort et al., 2008; He et al., 2010; Ray and Maunsell, 2010; Jensen and Mazaheri, 2010; Scheffer-Teixeira et al., 2012; Lisman and Jensen, 2013; Takeuchi et al., 2015; Richardson et al., 2017; Vaz et al., 2017; Helfrich et al., 2017, 2018; Gans et al., 2009; Mukamel et al., 2014; Purdon et al., 2013; Soplata et al., 2017; Voytek et al., 2010; Fell and Axmacher, 2011; Bergmann and Born, 2018) and pathological conditions (López-Azcárate et al., 2010; de Hemptinne et al., 2013, 2015; Schevon et al., 2013; Amiri et al., 2016; Cole et al., 2017; Ahnaou et al., 2017). In particular, Phase-to-Amplitude Coupling (PAC) is an important variant of the CFC phenomenon, in which the amplitude of a higher frequency band is modulated by the phase of another band with a lower frequency content. The PAC phenomenon has been reported to be involved in different processes between several frequency ranges, using various techniques for recording neuronal activity (Bragin et al., 1995; Lakatos et al., 2005, 2008; Canolty et al., 2006; Tort et al., 2008; He et al., 2010; Scheffer--Teixeira et al., 2012; Richardson et al., 2017; Vaz et al., 2017; Helfrich et al., 2017; López-Azcárate et al., 2010; de Hemptinne et al., 2013, 2015; Schevon et al., 2013; Amiri et al., 2016; Cole et al., 2017; Ahnaou et al., 2017) and algorithms for the quantification of the CFC (Kramer et al., 2008b; Penny et al., 2008; Onslow et al., 2011; Dvorak and Fenton, 2014).

Most of the pioneer works focused on the study of PAC in the context of neuronal rhythmic activity have been performed implicitly assuming sinusoidal oscillation, without taking into account the effects of nested frequency patterns that may emerge from nonsinusoidal or pseudoperiodic rhythms (Bragin et al., 1995; Lakatos et al., 2005, 2008; Canolty et al., 2006; Tort et al., 2008; He et al., 2010). More recently, it has been reported evidence showing that nested frequency patterns could also emerge from nonsinusoidal waveform shapes. In this case, high-frequency oscillations appear in the spectral decomposition as a consequence of the nonsinusoidality exhibited by the repeated pattern in the original signal; most importantly, the dependent (harmonically related) high-frequency oscillations are phase coupled to the slower rhythm (fundamental frequency) and the resulting spectral signature is similar to that of the PAC pattern (Kramer et al., 2008b; Aru et al., 2015; Jones, 2016). This aspect has attracted a lot of attention in the community (Vaz et al., 2017; Cole et al., 2017; Kramer et al., 2008b; Aru et al., 2015; van Driel et al., 2015; Jensen et al., 2016; Gerber et al., 2016; Lozano-Soldevilla et al., 2016; Cole and Voytek, 2017), as it challenges the functional interpretation of high-frequency oscillations as processes communicating relevant independent information; that is, the CFC observed at the signal level can be elicited by the interaction of two underlying neural oscillators, or it can be a consequence of the nonsinusoidal oscillations not necessarily produced by independent neural processes. Importantly, it has been experimentally shown that sinusoidal and nonsinusoidal brain activity both produce PAC (see Fig. 1); however, they reflect two distinct physiological neural mechanisms that are anatomically segregated in the human brain (Vaz et al., 2017). The reported algorithms specialized for the assessment of PAC can not distinguish between the different nested frequency types described above (Kramer et al., 2008b; Penny et al., 2008; Onslow et al., 2011; Dvorak and Fenton, 2014; van Driel et al., 2015; Jensen et al., 2016). Therefore, to elucidate the mechanisms underlying the CFC patterns observed at the signal level, the spectral characteristics of the associated neural activity should be considered.

Recent modeling and theoretical works have shown that PAC may be generated in several brain circuits with different architectures (Hyafil et al., 2015b; Onslow et al., 2014; Sotero, 2016). A common approach used in theoretical works is to keep the network topology as simple as possible in order to disentangle the minimal components of the phenomena under study. However, these topologies may be insufficient to properly describe a given anatomical network, the different spectral components that simultaneously should emerge, and their interaction. For example, in Parkinson's disease (PD), strong PAC has been observed in the local field potentials recorded from primary motor cortex. It has been found that in the parkinsonian state, cortical PAC is exaggerated compared to that observed in patients without movement disorders (de Hemptinne et al., 2013; Shimamoto et al., 2013). The reported evidence suggests that this excessive coupling is probably a manifestation of an excessive cortico-basal ganglia synchronization and may be related to motor dysfunction in PD. Although several works support the association of PAC with the parkinsonian state (de Hemptinne et al., 2013; Shimamoto et al., 2013; Connolly et al., 2015; van Wijk et al., 2016), the origin and type of PAC in this context, and the influence of the network architecture (Leblois et al., 2006; Schroll and Hamker, 2013; Velarde et al., 2017) have been insufficiently explored.

In this work, we study and characterize PAC patterns emerging from several basic architectures previously identified as biologically plausible neuronal circuits for the generation of nested frequency patterns (Hyafil et al., 2015b). Besides, we investigate the emergence of PAC in a model of neuronal populations inspired by previous basal ganglia models for the generation of pathological oscillations associated with PD. In the general case, we propose conditions under which PAC emerges in the presented architectures using tools of dynamical systems theory. In particular, we characterized CFC in the context of the bifurcation structure of the networks. As a consequence, the observed PAC may be considered as fingerprints of these generic bifurcations supported by the interaction between dynamics and network structure, and such universality stands independently of the physical nature of the process at hand.

In order to describe and quantify PAC in different conditions, we have characterized signals emerging from the population dynamics in several regimes using the Phase Locking Value (PLV) and the Modulation Index based on the Kullback-Leibler distance (KLMI), which are standard measures to quantify PAC (intensity and occurring phase). In addition, we introduce a new metric, the Time Locked Index (TLI), which quantifies the presence of harmonics in the Fourier spectrum of the signal.

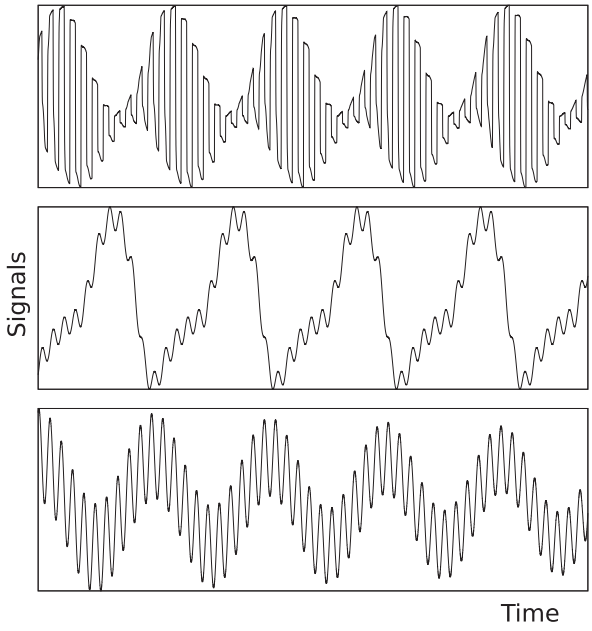

Fig. 1. Waveform shapes emerging from different physiological neural mechanisms wich confound the traditional metrics for the assessment of PAC. (Top) Amplitude of the fast oscillation is modulated by the phase of a slow oscillation. Note that in this case the fast and slow oscillatory dynamics are nonsinusoidal rhythms. (Center) Linear superposition of a nonsinusoidal slow oscillation and a fast oscillation. (Bottom) Linear superposition of two sinusoidal oscillations with different frequencies.

The theoretical analysis presented here makes use of these metrics to demonstrate that harmonic (aka: "spurious") and nonharmonic (aka: "true") PAC patterns naturally emerge from the interaction between neural populations in biologically plausible networks, as a signature of different bifurcation structures. The performance of the proposed method is shown for a variety of network architectures capable to produce different types of PAC, including a network model of the parkinsonian basal ganglia. It is worth noting that the interpretation of the CFC patterns observed at the signal level is a relevant unsolved problem which is currently under debate in the specialized literature (Aru et al., 2015; Cole and Voytek, 2017; Cole et al., 2017). In this regard, our results shed light on this challenging open issue contributing to a better understanding of the mechanism underlying the PAC patterns. In addition, our approach also defines a processing toolbox that can be used to investigate and interpret CFC patterns emerging in experimental data from many other scientific fields.

2. Network

2.1. Architecture

The dynamics of a network will be able to generate CFC only if it gives rise to at least two different frequencies that display some kind of interaction. Depending on the nature of the synaptic connection between neural oscillators, different CFC classes can be distinguished (Hyafil et al., 2015b). In the following sections we describe the analysis of CFC based on bifurcation theory for the BG-thalamocortical neural network the context of PD (Fig. 2). For the sake of clarity, the results of the proposed analysis corresponding to other four biologically plausible network architectures are included in Appendix A.

As described in Albin et al. (1989), motor symptoms of Parkinson's disease arise from basal ganglia dysfunction. The basal ganglia (BG) are a highly organized network constituted by four main subnuclei: striatum, globus pallidus (internal and external segments), subthalamic nucleus, and substantia nigra (compact and reticular). The BG network is critical for motor planning and action selection. It has several loops, where cortical and subcortical projections interact with internal reentry loops forming a complex network which is thought to be intended for selecting and inhibiting simultaneously occurring events and signals (Lanciego et al., 2012). Three main pathways (hyperdirect, direct, indirect) have been proposed for the transmission of signals through the basal ganglia (Nambu et al., 2002). These pathways have competing effects on movement and it is often assumed that a balance between them is involved in establishing and regulating muscle tone (Swenson, 2006). Indirect and hyperdirect pathways form negative feedback loops, while direct pathway gives rise a positive feedback loop (Leblois et al., 2006). In order to examine the dynamics of the BG-thalamocortical network, we propose a version of the pathophysiology model of PD. The proposed architecture is based in an alternative approach (Leblois et al., 2006) to the classical models of motor symptoms of PD (DeLong, 1990).

In Fig. 2, we present a mean-field model of BG-thalamocortical network whose firing rate dynamics is capable of generating PAC. The rationale behind the proposed model was based in two main constraints:

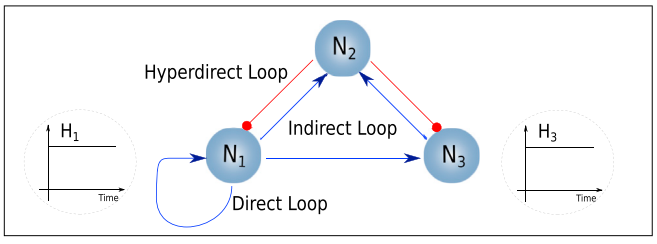

Fig. 2. BG-thalamocortical network for the generation of pathological oscillations associated with the parkinsonian state.

1) to include the three main loops (Indirect, direct and hyperdirect) hypothesized to be responsible of the pathophysiology dynamics of the BG-thalamocortical network (Albin et al., 1989; DeLong, 1990; Leblois et al., 2006) and 2) to use the minimum number of neuronal populations. Thus, we started by explicitly considering all the nuclei constituting the BG-thalamocortical network. Then, we minimize the number of neural populations by merging adjacent nuclei and adjusting the sign, efficacy, time constant and delay of the synaptic connections accordingly. As a result, we end up with a network model composed by three populations of neurons in which N_1 can be associated to the motor cortex and the loop N_2–N_3 representing the BG network. Thus, the populations N_2 and N_3 are not directly mapped to particular BG nuclei; however, the proposed architecture incorporates three loops that can be understood as the direct, indirect and hyperdirect loops of the BG-thalamocortical network. In Fig. 2, nodes 1 and 3 are constituted by excitatory neurons, while node 2 is a set of inhibitory neurons.

2.2. Dynamics

The BG-thalamocortical network dynamics is represented by a rate model (Wilson and Cowan, 1972). A node i is characterized by the instantaneous activity $A_i = S(I_i)$, where I_i is the total synaptic input to the population i and $S(I_i)$ is the nonlinear input-output transfer function. We considered threshold linear transfer functions, $S = [I_i]_+$.

The synaptic interaction from node i to node j is denoted by the variable m_{ij}, which is a low-pass filtered version of its instantaneous activity A_i (Shriki et al., 2003) and is described as follows,

$$\tau_{ij}\dot{m}_{ij} = -m_{ij} + A_i, \tag{1}$$

where τ_{ij} is the time constant of the synapses and the over-dot indicates derivative with respect to time.

The total synaptic input I_j received by population j is given by

$$I_j = \sum_{i \to j} G_{ij} m_{ij}(t - \Delta_{ij}) + H_j, \tag{2}$$

where Δ_{ij} and G_{ij} denote the synaptic delay and synaptic efficacy of the interaction $i \to j$, respectively. Each population j receives an external input given by H_j.

In this work, we are mainly interested to study the nonlinear interaction between two frequency bands (fast and slow oscillations) emerging from the biologically plausible models presented in Figs. 2 and 12. For this, the synaptic efficacies G_{ij} can be varied so that the system is in different dynamical states. Besides, by controlling the time constants and delays, the resulting oscillatory frequencies can be configured to belong to the α and γ bands or to the β and γ bands if necessary. All the parameters for the BG-thalamocortical network are summarized in Table 1.

3. Analysis

3.1. Bifurcations

We first characterized the stability of the solutions near the stationary state in the nonlinear delayed system. For this, we linearized the system of equations by proposing the solution $m_{ij} = \alpha_i + \beta_{ij}\exp(\lambda t)$, for the population i receiving inputs from population k and projecting onto the population j. We obtain that

$$\vec{\alpha} = S(\mathbb{G}^T\vec{\alpha} + \vec{H}), \tag{3}$$

and

$$0 = (1 + \lambda\tau_{ij})\beta_{ij} - \sum_k S'(S^{-1}(\alpha_i))G_{ki}\exp(-\lambda\Delta_{ki})\beta_{ki}, \tag{4}$$

where $\vec{\alpha} = (\alpha_i)$, $\vec{H} = (H_i)$, $\mathbb{G}^T = (G_{ij})$. The number of equations in system of equation (3) is equal to the number of populations, whereas in Eq. (4) it is equal to the number of connections. Eq. (3) allows to calculate the steady state, while Eq. (4) is used to evaluate the stability of the stationary state. For fixed parameters (G, τ, Δ) and inputs $\vec{H}$, the roots λ computed from Eq. (4) provide information about the solution near the steady state; it will be stable only if the real part of the roots are negative.

Due to the fact that we are using threshold linear transfer functions, $S = [I_i]_+$, we can use a linear approximation, justifiable when $\alpha_i > 0$ (activation conditions). For this transfer function, we obtained the factor

$$S'\left(S^{-1}(\alpha_i)\right) = \begin{cases} 1 & \alpha_i > 0 \\ 0 & \alpha_i < 0 \end{cases} \tag{5}$$

Let us note that a nonlinear transfer function S could significantly modify the bifurcation curves in the parameters space, since the synaptic connections in Eq. (4) are multiplied by the derivative of the transfer function S'.

If S is injective and continuously differentiable, then $G^*_{ki} = S'(S^{-1}(\alpha_i))$ G_{ki} is a change of variables of G_{ki} . This implies $\lambda = \lambda(\mathbb{G})$ is a continuous function. In other cases, the function $\lambda(\mathbb{G})$ could be discontinuous.

We found that in the general context of dynamical systems, and in particular for the biologically plausible networks presented in Figs. 2 and 12, several well defined mechanisms can produce the system dynamics to undergo oscillations with at least two different frequencies. The latter is a necessary, but not sufficient, condition for the emergence of CFC.

Specifically, we identify three type of transitions by which two rhythms oscillating at independent frequencies emerge in the system dynamics. The first mechanism involves the periodic excitation/inhibition of a network population (PEI) produced by an input received from another population pertaining to the same network (Figs. 2 and 12b and c) or by an external input (Fig. 12a). The other two transitions occur in a bifurcation point. In the second mechanism a system exhibiting an oscillatory dynamics undergoes a secondary bifurcation with a different frequency. This is called a Neimark-Sacker bifurcation, torus bifurcation or secondary Hopf (SH). In the third mechanism, a fixed point loses stability in connection with two pairs of complex eigenvalues (with different imaginary part) crossing the axis Re($\lambda = 0$) at the same time. This is a co-dimension 2 bifurcation called double Hopf or Hopf-Hopf (HH) (Izhikevich, 2014; Kuznetsov, 1998). To consider in detail the dynamics near each one of these bifurcations, let us start by defining the normal forms.

For the SH we analyzed the behavior of discrete-time systems obtained by using the Poincaré map (Kuznetsov, 1998). Let us consider the system

$$x \mapsto f(x, \alpha) \qquad x \in \mathbb{R}^2, \alpha \in \mathbb{R} \tag{6}$$

with a smooth function f, which has at $\alpha = 0$ the fixed point $x = 0$ with simple eigenvalues $\mu_{1,2} = (1 + \beta(\alpha))e^{\pm i\theta(\alpha)}$, $0 < \theta_0 < \pi$. By the introduction of a complex variable and a new parameter, the system can be transformed into

$$z \mapsto \mu(\beta)z + c_1(\beta)z|z|^2. \tag{7}$$

Then, near the fixed point the map (6) is locally conjugate to the normal form (7).

Following Kuznetsov (1998), to obtain the HH normal form we considered a smooth system depending on two parameters

$$\dot{x} = f(x, \alpha)\ x \in \mathbb{R}^4, \alpha \in \mathbb{R}^2 \tag{8}$$

which has, for $\alpha = 0$, the equilibrium $x = 0$ with eigenvalues

$$\lambda_k(\alpha) = \mu_k(\alpha) \pm i\omega_k(\alpha), \qquad k = 1, 2 \tag{9}$$

such that $\mu_k(0) = 0, \omega_k(0) > 0$.

Let the nondegeneracy conditions be satisfied (Kuznetsov, 1998). Then, the system is locally smoothly orbitally equivalent near the origin to the polar system

$$\begin{cases} \dot{r_k} = r_k\left(\mu_k + p_k r_k^2 + p_{kj} r_j^2 + s_k r_j^4\right) + \Phi_k \dot{\phi}_k = \omega_k(\alpha) + \Psi_k, & k \neq j \end{cases} \tag{10}$$

where μ_k, p_k, p_{kj} and s_k depend on α. In addition, $\Phi_k = O((r_1^2 + r_2^2)^3)$ and $\Psi_k = O(1)$. For more details about both bifurcations (SH and HH), we refer the reader to sections 4.6, 5.3 and 8.6 of Kuznetsov (1998).

To identify the mechanism eliciting PAC we analyzed the topological structure of the signals near the SH and HH bifurcations. Let us start by considering a stable limit cycle $\vec{x}_c(t)$ with fundamental frequency ω_1. It can be expressed by a Fourier series

$$\vec{x}_c(t) = \sum_n \vec{a}_n \cos(\omega_1 nt) + \vec{b}_n \sin(\omega_1 nt). \tag{11}$$

This expression shows that $\vec{x}_c$ is a superposition of harmonic oscillations, each contained in the plane generated by $\vec{a}_n$ and $\vec{b}_n$. Without loss of generality, we use only the fundamental term $n = 1$ and $\vec{a}_1 = \hat{x}$, $\vec{b}_1 = \hat{y}$.

In each point $\vec{x}_c(t)$, it is possible to define a orthonormal basis $\{\gamma(t), \kappa(t), \eta(t)\}$ where $\gamma(t)$ is tangent to the limit cycle and $\kappa(t), \eta(t)$ generate the orthogonal plane to $\gamma(t)$, Poincaré plane (see Fig. 3).

For the proposed case $n = 1$,

$$\begin{aligned} \gamma(t) &= -\sin(\omega_1 t)\hat{x} + \cos(\omega_1 t)\hat{y} \\ \kappa(t) &= \vec{x}_c(t) = \cos(\omega_1 t)\hat{x} + \sin(\omega_1 t)\hat{y} \\ \eta(t) &= \hat{z}. \end{aligned} \tag{12}$$

Given that the limit cycle is stable, the Poincaré map has a stable fixed point. The secondary Hopf bifurcation changes the stability of the point and it generates a closed invariant curve with frequency ω_2,

$$\begin{aligned} \vec{x}_{SH}(t) &= \vec{x}_c(t) + \Delta_2(t), \\ pt\Delta_2(t) &= \delta(\cos(\omega_2 t)\vec{x}_c(t) + \sin(\omega_2 t)\hat{z}). \end{aligned} \tag{13}$$

where $\delta \approx 0$. Note that Δ_2 is a sinusoidal oscillation with frequency ω_2 and its corresponding plane rotates with frequency ω_1. In a canonical basis, Eq. (13) is equivalent to

$$\begin{aligned} \begin{pmatrix} x \\ y \\ z \end{pmatrix} &= \begin{pmatrix} [1 + \delta\cos(\phi_2)]\cos(\phi_1) \\ [1 + \delta\cos(\phi_2)]\sin(\phi_1) \\ \delta\sin(\phi_2) \end{pmatrix}, \\ \phi_1 &= \omega_1 t, \\ \phi_2 &= \omega_2 t. \end{aligned} \tag{14}$$

Equation (14) indicates that $\vec{x}_{SH}$ is contained in a 2-dimensional torus (Fig. 4 top-left). The projection of $\vec{x}_{SH}$ onto the plane (x, y) is

Table 1
Values of the coupling parameters time constants and delays, for the BG-thalamocortical network.

	Synaptic efficacy	Delay	Time constant
	G	Δ (ms)	$\tau_{\alpha\alpha'}$ (ms)
1–1	0.5	35	40
1–2	(0,5)	35	40
1–3	(0,5)	5	20
2–1	−2.5	35	40
2–3	−1(*)/-0.7(**)	5	0.1
3–2	1.4	5	0.1

We call configuration A when $G_{23} = -1$ (*) and B when $G_{23} = -0.7$ (**). In both cases, we use $H_1 = 0.01$.

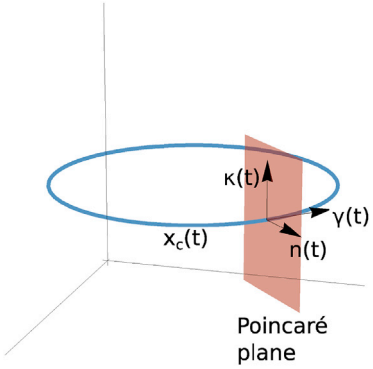

Fig. 3. Poincaré section for a limit cycle $\vec{x}_c(t)$. In each point of the limit cycle, it is possible to define a orthonormal basis $\{\gamma(t), \kappa(t), \eta(t)\}$ where $\gamma(t)$ is tangent to the limit cycle and $\kappa(t), \eta(t)$ generate the orthogonal plane to $\gamma(t)$ called Poincaré plane.

shown in Fig. 4 middle-left. We also plot one component (signal x) as a function of time in Fig. 4 bottom-left.

In contrast to SH, HH is a bifurcation of a fixed point of the dynamical system. The critical equilibrium has two pairs of purely imaginary eigenvalues. Near the bifurcation point of the parameter space, the linear solution is

$$\begin{aligned}\vec{x}_{HH}(t) = \vec{a}_1 \cos(\omega_1 t) + \vec{b}_1 \sin(\omega_1 t) \\ + \vec{a}_2 \cos(\omega_2 t) + \vec{b}_2 \sin(\omega_2 t).\end{aligned} \tag{15}$$

Taking into account that each harmonic component belongs to a different plane, the Fourier decomposition presented in Eq. (15) can be written in a canonical basis as follows,

$$\begin{aligned}\begin{pmatrix} x \\ y \\ z \end{pmatrix} = \begin{pmatrix} \cos(\phi_1) \\ \sin(\phi_1) \\ 0 \end{pmatrix} + \delta \begin{pmatrix} \cos(\phi_2) \\ \cos(\phi_2) \\ \sin(\phi_2) \end{pmatrix}, \quad \delta \in \mathbb{R}. \\ \phi_1 = \omega_1 t, \\ \phi_2 = \omega_2 t.\end{aligned} \tag{16}$$

The first term of the right-hand side of Eq. (16) is contained in the plane (x, y), while the second term belongs to the plane generated by $(1, 1, 0)$ and $\hat{z}$. Eq. (16) is a parametrization of a torus-shaped surface collapsed at two radially opposite regions (Fig. 4 top-right). This effect can be understood observing the oscillation planes. In the HH case, both planes of oscillations, corresponding to ω_1 and ω_2, are fixed. The plane associated to ω_2 is denoted by π. Since the planes are constant, there are two regions where π is tangent to the trajectory of the limit cycle corresponding to ω_1 (see Fig. 4 middle-right). Conversely, in the SH bifurcation the plane π rotates in the direction of the limit cycle (ω_1), being always perpendicular to its trajectory ($\vec{x}_c(t)$), as it is shown in Fig. 4 middle-left.

Importantly, our analysis of the system dynamics allows identifying specific bifurcation structures as the underlying mechanisms that satisfy the sufficient condition for producing PAC. It was useful in determining the system behavior (Fig. 4 top) and the structural differences between the resulting signals shown in Fig. 4 bottom. Specifically, near the SH bifurcation boundary the solution corresponds to a trajectory on a two-dimensional invariant torus (Fig. 4 top-left) and the one-dimensional projection x exhibits the complete structure of the PAC pattern, i.e. the modulating slow oscillation $\cos(\omega_1 t)$ superimposed to the amplitude modulated fast oscillation $\cos(\omega_1 t)\cos(\omega_2 t)$ (Fig. 4 bottom-left). On the other hand, the HH produces a linear superposition of the slow and fast oscillatory dynamics and no cross-frequency coupling occurs (Fig. 4 bottom-right). In this case, the complete solution is contained in a surface that is not topologically equivalent to a torus (Fig. 4 top-right).

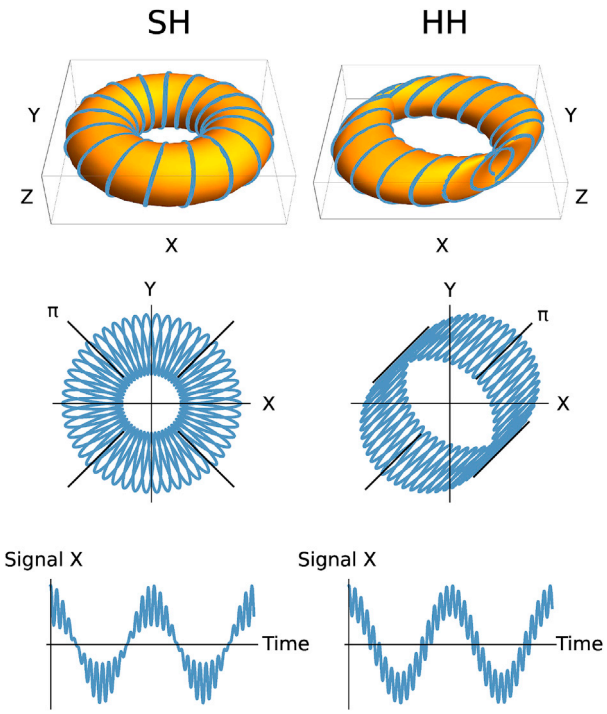

Fig. 4. Bifurcation structure. Left and right panels correspond to secondary and double Hopf bifurcations, respectively. (Top) Representation in phase space (x, y, z). (Middle) Projection in plane (x, y). (Bottom) Signal x as function of time.

It is worth noting that traditional methods for PAC quantification (Tort et al., 2010) (see Section III) can not distinguish between these mechanisms mainly due to the fact that they operate at the signal level, that is, on a single one-dimensional projection (Fig. 4 bottom) of the intrinsically multidimensional system dynamics (Fig. 4 top).

Let us note that in this analysis the slow frequency can be either ω_1 or ω_2. In the case of Fig. 4 the fast oscillatory rhythm correspond to ω_2. In the Results section we will also show the opposite case.

3.2. Cross-frequency coupling metrics

In this section, we present two nonparametric estimators to describe PAC in the different system configurations. While Phase Locking Value (PLV) specifies the intensity and phase occurrence of PAC, the Time Locked Index (TLI) is a novel measure we propose to quantify the presence of harmonics in the Fourier spectrum of signal. Thus, using this information, we can characterize the PAC pattern observed at the signal level in connection with the underlying bifurcation structure. An alternative PAC metric called Modulation Index based on the Kullback-Leibler distance (KLMI) is defined and contrasted with the PLV metric in Appendix B.

3.2.1. Phase Locking Value (PLV)

The Phase Locking Value (PLV) quantifies the phase synchronization between two narrow-band signals (Aydore et al., 2013). Consider a signal $x(t)$, which has been band-pass filtered at two frequency bands x_{LF} and x_{HF}. The PLV estimator is defined as

$$\text{PLV} = \frac{1}{N} \sum_{t=1}^{N} \exp(i \Delta\phi(t)) \tag{17}$$

where $\Delta\phi = \phi(x_{LF}) - \phi(A(x_{HF}))$. The functions $\phi(x)$ and $A(x)$ are the phase and amplitude of a signal x obtained using the Hilbert transform $\mathscr{H}(x)$,

$$A(x)(t) = \sqrt{x^2(t) + \mathscr{H}^2(x)(t)},$$
$$\phi(x)(t) = \arctan\left[\frac{\mathscr{H}(x)(t)}{x(t)}\right]. \quad (18)$$

The modulus of PLV takes values on [0,1] with 0 reflecting the case where there is no phase lock (for a sufficiently large number of samples N) and 1 when the relative phase of the two signals x_{LF} and $A(x_{HF})$ is constant along time. Thus, high PLV values ($|PLV| \approx 1$) are obtained in the cases in which the amplitude of the high frequency time series oscillates at the lower frequency (Huelsemann et al., 2018).

3.2.2. *Algorithm for the detection of non sinusoidal waveforms: Time Locked Index (TLI)*

We developed a specialized processing tool, called Time Locked Index (TLI), to efficiently quantify the harmonic content of the signals. The characterization of the degree of harmonicity is important given that nested oscillations with independent frequencies and nonsinusoidal brain activity both can elicit a similar signature in the Fourier spectrum. In particular, the traditional algorithms for PAC quantification (e.g. PLV, KLMI) are confounded by harmonically related spectral components associated to nonsinusoidal brain activity, reporting significant PAC levels in absence of independent frequency bands. In the TLI algorithm, time-locked averages are implemented to exploit the phase synchronization characterizing the band-pass filtered time series constituted by harmonic spectral components. The following steps describe the procedure to compute TLI (see Fig. 5).

1. The input signal x is band-pass filtered at the low (LF) and high (HF) frequency bands under analysis, producing the time series x_{LF} and x_{HF}, respectively. Z-score normalization is applied on x_{LF} and x_{HF}.
2. The time instants corresponding to the maximum amplitude of both time series, x_{LF} and x_{HF}, are identified in each period of the low frequency band (T_{LF}). These time values for the slow and fast oscillation peaks are recorded in the time vectors t_{LF} (red down-pointing triangles in Fig. 5) and t_{HF} (green up-pointing triangles in Fig. 5), respectively.
3. Epochs $E_{HF}^{t_{HF}}$ with a length equal to one period of the lower-frequency band (T_{LF}) and centered at fast oscillation peaks (t_{HF}) are extracted form the time series x_{HF}. These epochs are averaged to produce a single epoch $< E_{HF}^{t_{HF}} >$. Note that the latter is a time-locked averaging due to the fact that all the epochs $E_{HF}^{t_{HF}}$ are centered at the time instants t_{HF}.
4. Epochs $E_{HF}^{t_{LF}}$ with a length equal to one period of the lower-frequency band (T_{LF}) and centered at slow oscillation peaks (t_{LF}) are extracted form the time series x_{HF}. These epochs are averaged to produce a single epoch $< E_{HF}^{t_{LF}} >$. Note that the latter is a time-locked averaging due to the fact that all the epochs $E_{HF}^{t_{LF}}$ are centered at the time instants t_{LF}.
5. Finally, the TLI is computed as follows,

$$\mathrm{TLI} = \frac{\max(< E_{HF}^{t_{LF}} >) - \min(< E_{HF}^{t_{LF}} >)}{\max(< E_{HF}^{t_{HF}} >) - \min(\langle E_{HF}^{t_{HF}} >)}. \quad (19)$$

In the case that the time series x_{LF} and x_{HF} are predominantly constituted by harmonic spectral components, the fast and slow oscillations in time domain are characterized by a high degree of phase-locking. As a consequence, the amplitude of $< E_{HF}^{t_{LF}} >$ results comparable to that of the $< E_{HF}^{t_{HF}} >$ and so we obtain TLI ≈ 1. On the other hand, if the time series x_{LF} and x_{HF} are constituted by nonharmonic spectral components, the fast and slow oscillations are non phase-locked. Therefore, the amplitude of $< E_{HF}^{t_{LF}} >$ is averaged out to zero and TLI ≈ 0 is obtained for a sufficiently large number of samples (see Fig. 5). Of note, the phase synchronization between the band-pass filtered time series (x_{LF} and x_{HF}) can be assessed using the PLV metric; however, the TLI algorithm has two significant advantages: 1) The TLI algorithm does not require to know the harmonic ratio between the two frequency bands of interest. On the other hand, to compute the PLV you need to know this harmonic ratio, *a priori*, to evaluate phase-phase coupling. 2) The TLI is robust against variations of the bandwidth of the band-pass filters used to obtain the time series x_{LF} and x_{HF}. Thus, by operating in the time-domain the TLI reliably assess the degree of phase-locking, even in the case in which several spectral harmonics are included in the bandwidth of the filters used to obtain x_{LF} and x_{HF}.

An alternative method to characterize the harmonicity of the system dynamics is to compute the fractal dimension of the invariant set corresponding to the phase space (Guckenheimer and Holmes, 2002). In this case, the fractal dimension is expected to be lower in the case of oscillatory dynamics including harmonically related frequencies than those constituted by independent frequency bands. However, this method requires processing data in several dimensions and is more computationally expensive than the TLI algorithm.

In all the cases reported in this work, the same configuration for the band-pass filters was used to compute the PLV, KLMI and TLI metrics. Besides, additive white Gaussian noise was added to the dynamics obtained from our firing-rate models prior to compute the PLV, KLMI (see Appendix A) and TLI metrics. The noise amplitude was set to the 10% of the standard deviation of the simulated time series.

In Appendix C, we present the analysis of simple nonlinear oscillator to illustrate the behavior of the measures that characterize the cross-frequency coupling (PLV, KLMI) and harmonicity (TLI). The source code for TLI computation and a test script example associated to the results shown in Appendix C are available at https://github.com/damian-dellavale/Time-Locked-Index/.

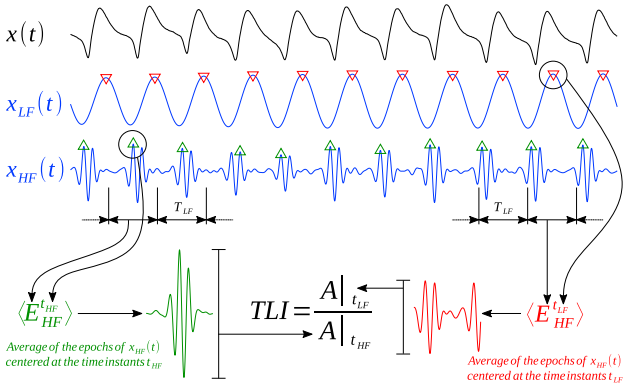

Fig. 5. Schematic representation of the algorithm to compute the TLI (see description in the text).

4. Results

In this section, we show the results corresponding to the BG-thalamocortical network model (see Fig. 2). We analyzed the behavior of the system as a function of the synaptic efficacies of the connections (G_{ij}). In particular, we study the effect of the indirect (G_{13}) and hyperdirect (G_{12}) pathways in the parameter space (G_{12}, G_{13}).

First, we calculate the fixed points of the network dynamics using Eq. (3)

$$\begin{bmatrix} \alpha_1 \\ \alpha_2 \\ \alpha_3 \end{bmatrix} = \frac{1}{D} \begin{bmatrix} H_1(G_s - 1) + H_3 G_{32} G_{21} \\ -H_1(G_{12} + G_{13}G_{32}) - H_3(1 - G_d)G_{32} \\ -H_1(G_{13} + G_{12}G_{23}) - H_3(1 - G_d - G_h) \end{bmatrix} \quad (20)$$

where

$$
\begin{aligned}
D &= (1 - G_d)(G_s - 1) + G_h + G_i \\
G_d &= G_{11} \\
G_h &= G_{12}G_{21} \\
G_s &= G_{23}G_{32} \\
G_i &= G_{13}G_{32}G_{21}
\end{aligned}
\tag{21}
$$

It is found that for $G_{11} < 1$, $\alpha_1, \alpha_2 > 0$ for all (G_{12}, G_{13}). Similarly, the activation condition for the node 3 ($\alpha_3 > 0$) is

$$
G_{13} > G_{12}\left(\frac{H_3}{H_1}G_{21} - G_{23}\right) - \frac{H_3}{H_1}(1 - G_d). \tag{22}
$$

Eq. (22) defines two half-planes in the parameters space. In both of them, the stability of the fixed points is controlled by the roots of the characteristic equation $p(\lambda) = 0$ where

$$
p(\lambda) = \begin{cases} \Gamma_1(\lambda) - \Gamma_2(\lambda)G_s e^{-\Delta_s\lambda} - \Gamma_3(\lambda)G_i e^{-\Delta_i\lambda} - \\ \Gamma_4(\lambda)G_h e^{-\Delta_h\lambda}, & \alpha_3 > 0 \\ \Gamma_1(\lambda) - \Gamma_4(\lambda)G_h e^{-\Delta_h\lambda}, & \alpha_3 \leq 0. \end{cases} \tag{23}
$$

where

$$
\begin{aligned}
&\Gamma_d(\lambda) = (1 + \lambda\tau_{11} - G_d e^{-\Delta_d\lambda}), \\
&\Gamma_1(\lambda) = \Gamma_d(\lambda)(1 + \lambda\tau_{12})(1 + \lambda\tau_{13})(1 + \lambda\tau_{21}) \\
&(1 + \lambda\tau_{23})(1 + \lambda\tau_{32}), \\
&\Gamma_2(\lambda) = \Gamma_d(\lambda)(1 + \lambda\tau_{12})(1 + \lambda\tau_{21})(1 + \lambda\tau_{13}), \\
&\Gamma_3(\lambda) = \Gamma_d(\lambda)(1 + \lambda\tau_{12})(1 + \lambda\tau_{23}), \\
&\Gamma_4(\lambda) = \Gamma_d(\lambda)(1 + \lambda\tau_{13})(1 + \lambda\tau_{23})(1 + \lambda\tau_{32}).
\end{aligned}
\tag{24}
$$

The functions Γ_i depend only on the time constants τ and G_d. Note that when the population N_3 is not active (i.e. $\alpha_3 \leq 0$), the stability equation (23) is equivalent to a unique oscillator constituted by the populations N_1 and N_2.

To illustrate different bifurcation scenarios emerging from the BG-thalamocortical network dynamics, we use the parameter values presented in Table 1 to setup the configurations A and B corresponding to $G_{23} = -1$ and $G_{23} = -0.7$, respectively.

Fig. 6 shows the bifurcation diagram of the BG-thalamocortical network for configuration A. For $G_{12} \geq G_{13}$, the node N_3 is not active ($\alpha_3 \leq 0$). In this case, if G_{12} is sufficiently small ($\lesssim 0.7$), the system converges to a steady state. This implies the absence of oscillatory components in any signal. When G_{12} increases, the network is led to a oscillatory state through a Hopf bifurcation (arrow b in Fig. 6). The bifurcation curve and the characteristic frequency $\omega_{SO} \approx 4$ Hz were determined by solving the equation $p(2\pi i\omega) = 0$ numerically. Given that the node N_3 is inactive, the bifurcation curve is independent of the value of G_{13}.

According to Eq. (5), on the boundary of the half plane $G_{12} = G_{13}$, the derivative $S'(x)$ is not defined. As a result, there is a pair conjugated roots $\lambda = \mathrm{Re}(\lambda) \pm 2\pi i\omega_{FO}$ such that $\mathrm{Re}(\lambda)$ is a discontinuous function of the synaptic efficacies. In particular, as N_3 becomes active ($\alpha_3 > 0$), $\mathrm{Re}(\lambda)$ changes its sign destabilizing the system (arrow a in Fig. 6). The result of this transition is the formation of a limit cycle with characteristic frequency $\omega_{FO} \approx 50$ Hz. It is important to remark that this mechanism for generating a limit cycle does not imply a Hopf bifurcation.

We analyzed the evolution of the system dynamics using a Poincaré map (Kuznetsov, 1998). When G_{13} increases enough, the limit cycle (ω_{FO}) is destabilized by a SH bifurcation (arrow c in Fig. 6). This bifurcation corresponds to the case when the multipliers associated to the limit cycle (ω_{FO}) in the Poincaré map are complex and lie on the unit circle (Kuznetsov, 1998). As a consequence, the fixed point in the Poincaré map gives rise to a closed invariant curve with characteristic frequency $\omega_{SO} \approx 4$ Hz. The formation of the periodic orbit in the Poincaré plane ($I_3 = 0$) is presented in Fig. 7. In Fig. 7 we also show the state of the system (I_1, I_2, I_3) during the transition. The box (a) in Fig. 7 corresponds to a 50 Hz oscillation before the bifurcation, (b)-(c) are intermediate regimes and (d) exhibits the state after the SH bifurcation (see Fig. 6c). In the phase space (I_1, I_2, I_3) shown in Fig. 7, the SH generates a trajectory on a two-dimensional invariant torus with two characteristic frequencies ω_{FO} and ω_{SO}. Besides, the SH bifurcation is determined by the normal form coefficients of the restricted Poincaré map at the critical parameter values (Eq. (7)). The numerical results shown in Figs. 6c and 7 reproduce the characteristics of the SH bifurcation determined analytically in Eqs. (6)–(14). In particular, near the bifurcation boundary, the temporal evolution of the components I_1, I_2 and I_3 exhibit the complete structure of the PAC pattern, that is, the modulating slow oscillation superimposed to the amplitude modulated fast oscillation. The corresponding spectral signature was verified through a Fourier analysis (power spectra not shown).

In Fig. 6, the network displays oscillatory activity (ω_{SO}) for $G_{12} > 0.7$ and $G_{13} \approx 0$. For a given G_{13} value indicated by the arrow (d) in Fig. 6, the population N_3 is periodically activated around the maximum amplitude of the slow oscillation (ω_{SO}). As a consequence, the fast oscillation (ω_{FO}) emerges around that particular phase and remains silent in the rest of the slow oscillation cycle. This mechanism involving the periodic excitation/inhibition (PEI) of a network population, elicit the complete structure of the PAC pattern at the signal level and it was also observed in the network shown in Fig. 12a (See Appendix A.1).

In the case of the configuration B (see Table 1), the activation

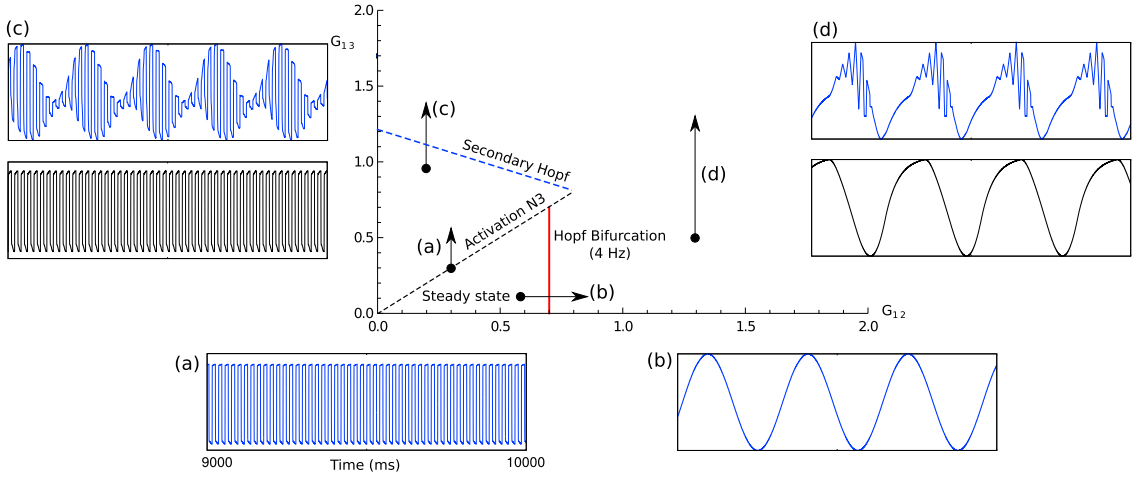

Fig. 6. Bifurcation structure of BG-thalamocortical network in configuration A. (a) Generation of a fast oscillation ($\omega_{FO} \approx 50$ Hz) via the activation of node N_3. (b) Hopf bifurcation destabilizes the system and a slow oscillation ($\omega_{SO} \approx 4$ Hz) appears. c) In SH, the limit cycle losses stability and a new oscillation with frequency ω_{SO} appears. d) If G_{13} increases, in a part of the period of the slow oscillation, there is superposition with a fast oscillation. All boxes show the signal I_3 as function of time in the range from 9000 to 10000 ms.

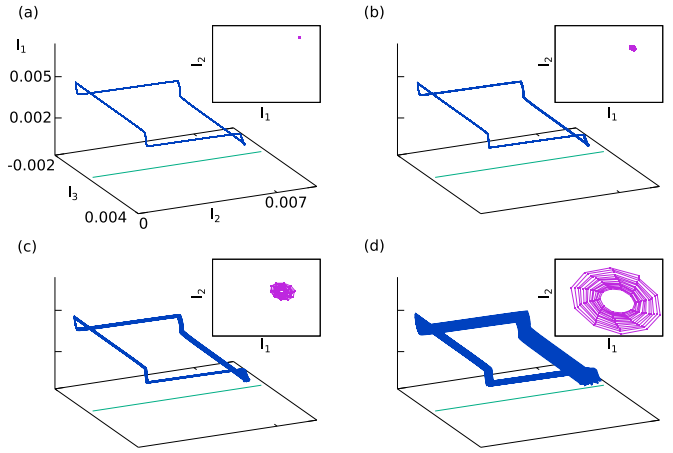

Fig. 7. Secondary Hopf bifurcation corresponding to arrow (c) in Fig. 6. The behavior of a periodic orbit in the space (I_1, I_2, I_3) can be represented in a Poincaré map ($I_3 = 0$). (a) Limit cycle and fixed point in the map are stable. (b)(c) Limit cycle and fixed point change stability. In the Poincaré map, this bifurcation is a discrete version of Hopf. (d) An invariant torus is formed. The intersection of the torus with the Poincaré plane corresponds to a closed invariant curve. All the graphics have the same scale.

condition for the node 3 ($\alpha_3 > 0$, Eq. (22)) is satisfied in the whole explored range of synaptic efficacies (G_{12}, G_{13}). In Fig. 8, we show the bifurcation structure corresponding to this configuration. Similarly to the previous results, when G_{12} increases, a periodic solution (ω_{SO}) arises via a Hopf bifurcation (point b in Fig. 8). Note that, for small values of G_{12}, increasing G_{13} elicits the formation of a limit cycle (with frequency ω_{FO}) without implying the activation of node N_3, as in the configuration A, but via a Hopf bifurcation (point a in Fig. 8).

In Fig. 8, the intersection point between the two Hopf curves determines a new transition called Hopf-Hopf bifurcation (point c in Fig. 8). The HH bifurcation represents the situation where two pairs of conjugate eigenvalues cross the imaginary axis at the same time. The truncated normal form of the HH bifurcation (Eq. (10)), indicates that the amplitude and phases of the two oscillations (ω_{SO}, ω_{FO}) are uncoupled. Near the transition point, we can approximate the solution as a superposition of two sinusoidal oscillations $A_{SO}\cos(\omega_{SO}t) + A_{FO}\cos(\omega_{FO}t)$. In general, for values of the parameters (G_{12}, G_{13}) far from the HH bifurcation, the nonlinear effects modify the dynamics giving rise to the appearance of a high harmonic content in the observed signals (point d in Fig. 8).

The PLV estimator computed from the signal I_3 is shown, as a function of the synaptic efficacies (G_{12}, G_{13}), in the colormaps of Fig. 9 for configurations A and B. The pseudocolor scale represents the |PLV| values ranging from 0 (blue) to 1 (red). In computing the PLV KLMI and TLI, the band-pass filters were configured with a null-to-null bandwidth of 1–19 Hz (to obtain x_{LF}) and 20–200 Hz (to obtain x_{HF}) which include the characteristic frequencies $\omega_{SO} \approx 4$ Hz and $\omega_{FO} \approx 50$ Hz, respectively. In Fig. 9, the regions in white color represent undefined PLV values corresponding to the nonoscillatory dynamics (stable steady state regions). On the other hand, nearby the formation of a limit cycle via the activation of the node 3 (arrow a in Fig. 9) or Hopf bifurcation (arrow b in Fig. 9), we obtain small PLV values ($|\text{PLV}| < 0.2$) indicating the absence of significant PAC associated with the occurrence of these mechanisms.

In both configurations presented in Fig. 9, the secondary Hopf bifurcation (SH) gives rise to a discontinuous jump in the |PLV| values. For example, in the phase space region indicated by the arrow (c), the |PLV| increases from 0 to 0.9 when the SH boundary is crossed. In contrast, the transition associated to the PEI mechanism indicated by the arrow (d), is characterized by a continuous variation of the |PLV| values. The latter is a consequence of the continuous increasing of the amplitude of the intermittent fast oscillations (ω_{FO}).

Note that near the HH (see Fig. 9 right), PLV vanishes because the signal I_3 is the sum of uncoupled oscillations without CFC. In Fig. 9, the region circumscribed above the Hopf bifurcations and below the SH bifurcations is characterized by low PLV values ($|\text{PLV}| < 0.2$) and a variety of waveform shapes like sinusoidal oscillations (Fig. 8a), sum of uncoupled oscillations (Fig. 8c) and nonsinusoidal waveforms (Fig. 8d).

In Fig. 9 right, the dashed white lines mark a secondary Hopf bifurcation occurring nearby the Hopf bifurcations (HH). This result was confirmed using a Poincaré map and is consistent with the analysis of the truncated normal form of the HH bifurcation presented in Kuznetsov (1998). In Ref. Kuznetsov (1998) it is shown that a generic four-dimensional system exhibiting a HH also has the corresponding SH bifurcation curves in its parametric portrait near this codimension 2 point. Crossing these curves elicit the occurrence of limit cycles (Hopf bifurcations) and invariant two-dimensional tori nearby (secondary Hopf). For generic parameter values, the orbit structure on a torus depends on the distance to the secondary Hopf curve. The tori exist and remain smooth only near the bifurcation curves. Otherwise, tori lose smoothness and are eventually destroyed.

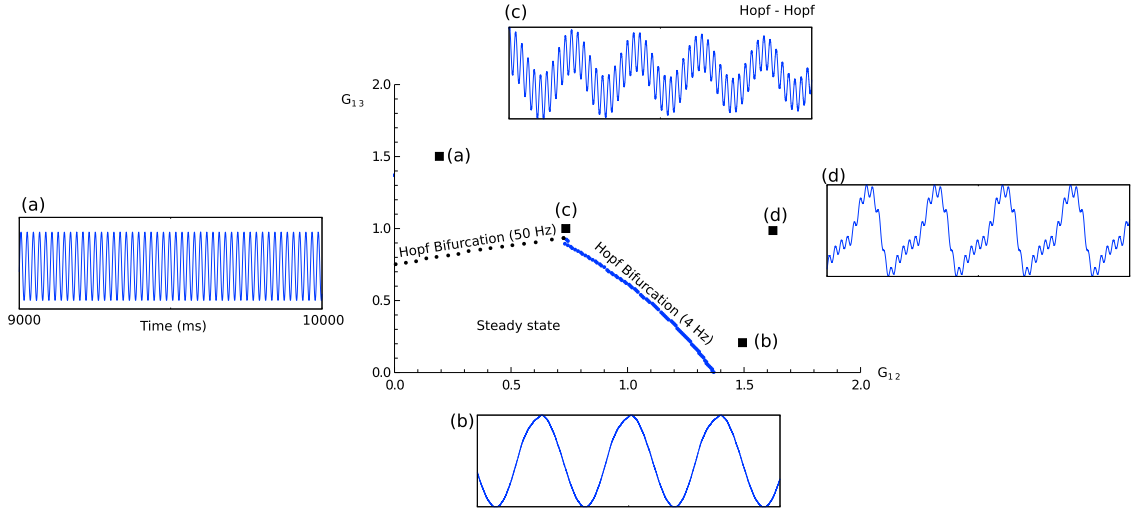

Fig. 8. Bifurcation structure of BG-thalamocortical network in configuration B. (a) Hopf bifurcation corresponding to a fast oscillations ($\omega_{FO} \approx 50$ Hz). (b) Hopf bifurcation corresponding to slow oscillations ($\omega_{SO} \approx 4$ Hz). (c) Hopf-Hopf bifurcation occurs at the intersection of the two Hopf branches. The solution is a sum of uncoupled sinusoidal signals. Away from the bifurcation, the signal changes its shape. (d) Nonlinear effects give rise to the appearance of nonsinusoidal waveforms. In all boxes. signal I_3 is shown as a function of time in the range from 9000 to 10000 ms.

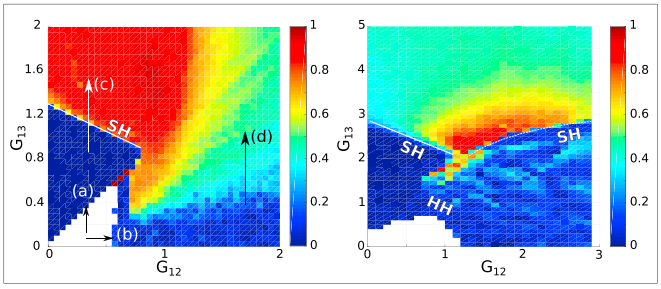

Fig. 9. Absolute value of PLV as a function of the synaptic efficacies (G_{12}, G_{13}). Left and right panels correspond to configurations A and B of BG-thalamocortical network (Fig. 2), respectively. Dashed lines mark secondary Hopf bifurcation (SH). Arrow (a) and (b) indicate the formation of limit cycle via activation or Hopf bifurcation, respectively. Arrows (c) and (d) show discontinuous and continuous variations of PLV, respectively. White regions correspond to steady states. In both cases, PLV was computed for the signal I_3.

We characterized the degree of harmonicity of the slow oscillations (fundamental frequency ω_{SO}) using the TLI algorithm. In Fig. 10, the TLI is shown as a function of the parameters (G_{12}, G_{13}) for configurations A and B.

For the configuration A (Fig. 10 left), the region circumscribed above the activation of the population N_3 and below the SH boundary is characterized by the presence of fast oscillation resulting in low TLI values (TLI<0.4) due to the absence of harmonics of the slow oscillation (ω_{SO}). On the other hand, at the right of the Hopf bifurcation (arrow b in Fig. 10) and above the SH boundary (arrow c in Fig. 10) higher TLI values are obtained (TLI $>$ 0.5) indicating that both transitions elicit nonsinusoidal slow oscillations (fundamental frequency: ω_{SO}) constituted by the superposition of harmonically related spectral components (see corresponding boxes in Fig. 6).

In the configuration B (Fig. 10 right), high TLI values (TLI $\approx$ 0.5) are observed crossing the Hopf bifurcation at the right due to the fact that it produces nonsinusoidal slow oscillations (fundamental frequency: ω_{SO}). High TLI values (TLI $>$ 0.5) are also observed in some regions above the SH boundaries for configuration B.

The analysis of the PAC intensity (PLV map in Fig. 9 and KLMI map in Fig. 17) and the harmonicity of the slow oscillations (TLI map in Fig. 10) demonstrate that nested oscillations with independent frequencies ("true" nonharmonic PAC) and nonsinusoidal slow oscillations constituted by harmonically related spectral components ("spurious" harmonic PAC) both produce significant PLV and KLMI values and are indistinguishable for the traditional PAC algorithms. Importantly, in most of the phase space regions where the "true" nonharmonic PAC is observed, it coexist with the presence of harmonics of the slow oscillations

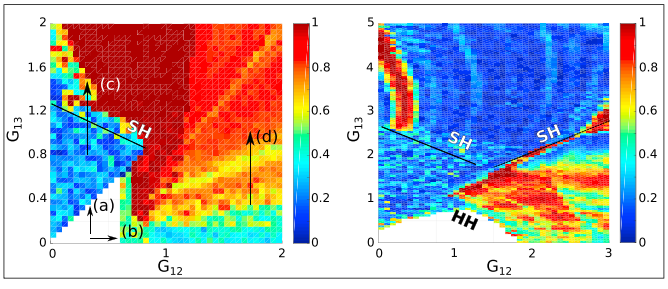

Fig. 10. Time Locked Index as a function of the synaptic efficacies (G_{12}, G_{13}). Left and right panels correspond to configurations A and B of BG-thalamocortical network (Fig. 2), respectively. Dashed lines mark secondary Hopf bifurcation (SH). Arrow (a) and (b) indicate the formation of limit cycle via activation or Hopf bifurcation, respectively. Arrows (c) and (d) show discontinuous and continuous variations of TLI, respectively. White regions correspond to steady states. In both cases, TLI was computed for the signal I_3.

("spurious" harmonic PAC).

The connection between the PAC observed at the signal level and the underlying bifurcation structure for the BG-thalamocortical network model is shown in Fig. 11 by means of projections of the complete multidimensional dynamics. Left and right panels correspond to HH and SH bifurcations, respectively. Top boxes show the solution of system in the space (I_1, I_2, I_3). In the middle, we project the signal to a plane. In the bottom graphs, the one-dimensional projection corresponding to the signals I_3 are shown as functions of time.

Supplementary video related to this article can be found at https://doi.org/10.1016/j.neuroimage.2019.116031.

We found that nonsinusoidal oscillatory dynamics constituted by the linear superposition of either uncoupled oscillations (HH bifurcation, Fig. 4 right-top, Fig. 8c) or harmonically related spectral components elicited by the action of nonlinear effects (Fig. 11 right, Fig. 8d) share a common signature in their space state representation: the geometrical shape of the invariant set is given by a torus-shaped surface collapsed at two radially opposite regions. This behavior can be understood using Eqs. (11) and (15). That is, the nonsinusoidal signal has at least one harmonic term $\omega' = \omega_1 n$ added to the oscillation ω_1 (see Eq. (11)). In this case, the resulting expression is equivalent to Eq. (15) with $\omega_2 = \omega'$, where each oscillation belongs to fixed planes. The latter, in turn produces the invariant torus-shaped surface collapsed at two radially opposite regions.

On the contrary, we found that SH bifurcation and PEI mechanisms both produce "true" nonharmonic PAC and are characterized by invariant sets given by a torus (Fig. 4 left-top, Fig. 11 left-top) and a closed trajectory (limit cycle of the slow oscillation) interleaved with a "bump" produced by the orbits of the intermittent fast oscillation (data not shown), respectively.

Hence, our results show that the mechanisms eliciting harmonic and nonharmonic PAC patterns are associated to invariant sets that are not topologically equivalent. This suggests that the signatures identified in the invariant sets could be used as a tool to identify the underlying

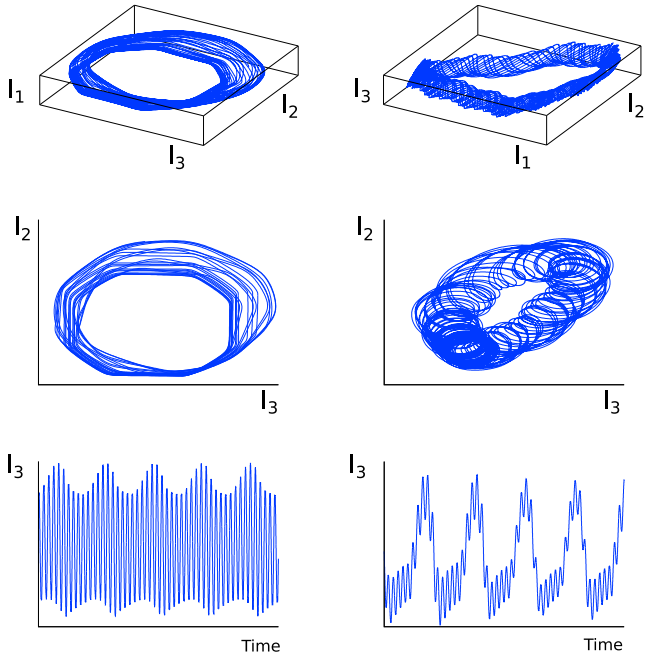

Fig. 11. Simulation results for configuration B of the network shown in Fig. 2. Left and right panels correspond to signals near the secondary (SH) and double Hopf bifurcation (HH), respectively. (Top) Representation in phase space (I_1, I_2, I_3). (Center) Projection in a plane (I_3, I_2). (Bottom) Signal I_3 as function of time. In parameter space $(G_{12}, G13)$ (see Figs. 9 and 10), left and right panels are associated with the points $(1.5, 2.5)$ and $(1.5, 1.5)$, respectively. A video showing the formation of these structures is included as Supplementary material.

mechanisms associated to the PAC phenomenon and to discriminate PAC patterns observed at the signal level that confound the traditional CFC algorithms.

5. Discussion

CFC is a rather ubiquitous phenomenon that has been observed in a variety of physical domains (Dellavale and Rossell, 2019; Walker et al., 2010; Dietrich et al., 2012; Hoermann et al., 2015; Ieva et al., 2013; Yang and Lin, 2005; Laskar et al., 2014; Eswaraiah et al., 2018; Paluš, 2014; Hathaway, 2010; Shapoval et al., 2017). In particular, the PAC variant of CFC has been reported to play an important role in several neural processes (Fries, 2005; Jensen and Colgin, 2007; Canolty and Knight, 2010; Hyafil et al., 2015b; Bragin et al., 1995; Lakatos et al., 2005, 2008; Palva et al., 2005; Canolty et al., 2006; Tort et al., 2008; He et al., 2010; Ray and Maunsell, 2010; Jensen and Mazaheri, 2010; Scheffer-Teixeira et al., 2012; Lisman and Jensen, 2013; Takeuchi et al., 2015; Richardson et al., 2017; Vaz et al., 2017; Helfrich et al., 2017, 2018; Gans et al., 2009; Mukamel et al., 2014; Purdon et al., 2013; Soplata et al., 2017; Voytek et al., 2010; Fell and Axmacher, 2011; Bergmann and Born, 2018; López-Azcárate et al., 2010; de Hemptinne et al., 2013, 2015; Schevon et al., 2013; Amiri et al., 2016; Cole et al., 2017; Ahnaou et al., 2017); however, the mechanisms underlying the emergence of PAC have been poorly explored in this context. In addition, nested frequency patterns could emerge from oscillatory neural activity due to the presence of independent frequency bands (nonharmonic PAC) or nonsinusoidal waveform shapes characterized by the presence of dependent, harmonically related, spectral components (harmonic PAC). The traditional algorithms to assess PAC (e.g. PLV, KLMI) (Tort et al., 2010) can not distinguish between these two different nested frequency types, reporting significant PAC levels even in absence of independent frequency bands (Kramer et al., 2008b; Penny et al., 2008; Onslow et al., 2011; Dvorak and Fenton, 2014; van Driel et al., 2015; Jensen et al., 2016). The latter is a major open issue since it has been experimentally shown that sinusoidal and nonsinusoidal brain activity both produce PAC; however, they reflect two distinct physiological neural mechanisms that are anatomically segregated in the human brain (Vaz et al., 2017).

In this work we determine the sufficient conditions under which CFC emerges in a system dynamics, as a signature of specific bifurcation structures. For this, we use analytical and numerical tools from the theory of dynamical systems to analyze the biologically plausible networks shown in Figs. 2 and 12. The model (12a) has been tested in the context of visual processing, where the pyramidal-interneuron oscillator responds to visual activity experimentally recorded in monkey thalamus (Mazzoni et al., 2008). The network (12b) has been proposed to model speech perception in auditory cortex using two separate sub-populations responsible for the generation of independent frequencies (Hyafil et al., 2015a). The architecture (12c) was used to model coupled θ-γ oscillations in hippocampus, which featured two interconnected sub-populations with distinct GABA decay time (White et al., 2000). In other context, architecture (12c) was also used to interpret the dynamics of local field potentials recorded from *in vitro* cortical slices as the interaction of superficial and deep layers (Kramer et al., 2008a). The model (12d) has been proposed to explain the emergence of θ-γ coupled oscillations in hippocampus, where a common population is coupled to fast-spiking cells and oriens-lacunosum moleculare cells (Wulff et al., 2009). The main results obtained through the bifurcation analysis of these networks are presented in Appendix A. It is worth noting that the proposed BG-thalamocortical network (Fig. 2) obtained by merging adjacent nuclei of the complete architecture, results to be a combination of these canonical structures (Fig. 12a–d).

In the theory of dynamical systems, a bifurcation occurs when a small smooth change made to the parameter values of a system causes a sudden topological change in its behavior. In the network architectures shown in Figs. 2 and 12, we observed three different bifurcations associated to the emergence of oscillatory dynamics: Hopf (H), double Hopf (HH) and secondary Hopf (SH). The Hopf bifurcation causes a fixed point to lose stability and a limit cycle with small-amplitude is created from the fixed point. This causes the appearance of a particular oscillation frequency (see Figs. 6 and 8 and Appendix D). The HH bifurcation corresponds to a critical point in a two-parameter family of autonomous differential equations at which two pairs of purely imaginary eigenvalues merge (Eq. (9)). The bifurcation point in the parameter plane lies at a transversal intersection of two Hopf bifurcation curves (Fig. 8). In discrete time systems (maps), Neimark-Sacker (NS) bifurcation is the birth of a closed invariant curve from a fixed point, when the fixed point changes stability via a pair of complex eigenvalues with unit modulus. In other words, NS bifurcation is a discrete version of Hopf bifurcation (Eq. (7)). The essential feature of a SH bifurcation is the occurrence of a NS bifurcation in the Poincaré map, and an invariant two-dimensional torus in the full system (Figs. 4 and 7). Importantly, the SH bifurcation is always present near a HH bifurcation (right graph in Fig. 9) (Kuznetsov, 1998).

In order to describe PAC in the different conditions, we have characterized the signals emerging from the population dynamics in different regimes using the Phase Locking Value (PLV) and the Modulation Index based on the Kullback-Leibler distance (KLMI). In addition, we have introduced a new metric, the Time Locked Index (TLI), which quantifies the presence of harmonic components in the power spectrum of the time series. The theoretical analysis presented here exploits these metrics to demonstrate that harmonic and nonharmonic PAC patterns naturally emerge from the interaction between neural populations as a signature of specific bifurcation structures.

In the context of the biologically plausible networks depicted in Figs. 2 and 12, we found three mechanisms eliciting co-ocurrent oscillations in the system dynamics, whose spectral power is concentrated in well-defined independent frequency bands: 1) Hopf-Hopf (HH) bifurcation producing a linear superposition of two uncoupled oscillations (see Fig. 8c). 2) Secondary Hopf (SH) bifurcation producing two phase-amplitude coupled oscillatory dynamics (see Fig.. 6c and 11 left). 3) Mechanisms involving periodic excitation/inhibition (PEI) of a network population (see Fig. 6d). Importantly, of the three aforementioned transitions occurring in the network dynamics only the SH bifurcation and the PEI mechanism involve phase-amplitude coupling of independent frequencies (i.e. “true” nonharmonic PAC). The SH bifurcation was observed in the BG-thalamocortical network model shown in Fig. 2 for both configurations A and B. Of note, the SH bifurcation is always present near the HH bifurcation (Kuznetsov, 1998), as it was observed in the configuration B (Fig. 9 right). On the other hand, the PEI mechanism was observed in network architectures shown in Fig. 2 (see Figs. 6d), 12a (see Figs. 13), 12b (see Figs. 14) and 12c (see Fig. 15). It is worth noting that the PEI mechanism elicit a PAC pattern characterized by intermittent fast oscillations (intermittent PAC).

When considering the linear regime with pure sinusoidal oscillatory dynamics near the bifurcations (TLI≈0), the SH and PEI mechanisms give rise to phase-amplitude coupled sinusoidal oscillations (nonharmonic PAC). In contrast, the HH bifurcation produces the linear superposition of two uncoupled sinusoidal oscillations with no CFC. In general, far enough from the boundaries corresponding to the mechanisms HH, SH and PEI, the non-linear effects can cause the emergence of harmonically related spectral components superimposed to the original sinusoidal oscillations, resulting in a system dynamics characterized by nonsinusoidal oscillations (TLI≈1). Under these nonlinear regime, the results shown in Figs. 9 and 10,17, 14 and 16 demonstrate that the traditional PAC algorithms based on linear filtering (e.g. PLV, KLMI) (Tort et al., 2010) can not distinguish between the “spurious” harmonic PAC present around the HH bifurcation and the more complex scenarios corresponding to SH and PEI mechanisms in which there is a combination of harmonic PAC and “true” nonharmonic PAC.

These results suggest that similar nonsinusoidal waveform shapes (Fig. 1) emerging from the oscillatory dynamics of biologically plausible networks can be associated to essentially different underlying scenarios, either with the presence of harmonically related spectral components

generated by a single nonlinear oscillator, or with the presence of independent frequency bands that are (phase-amplitude) coupled, or a combination of both. In addition, we found that a SH bifurcation involving two oscillations with close frequencies ($\omega_{FO} \approx 2\omega_{SO}$) elicit a periodic waveform shape having essentially the same features of that obtained from a different underlying mechanism such as the linear superposition of the same two oscillations (data not shown). Although having evident differences in their Fourier spectra, these two scenarios are hardly distinguishable in the time domain by analyzing the waveform shape. Taking together, these results point out that parametric and nonparametric methods to characterize CFC operating at the signal level, like those based on linear filtering or the waveform shape analysis, suffer from rather fundamental limitations to identify the underlying mechanisms of CFC, due to the fact that they operate on a single one-dimensional projection of an intrinsically multidimensional system dynamics.

Importantly, the geometrical shape of the invariant sets in the phase space corresponding to the identified bifurcations (see Figs. 4 and 11: HH and SH) present essential differences irrespective of the dynamical regime (sinusoidal or nonsinusoidal oscillations). These topological signatures could be exploited to identify the underlying PAC mechanisms by reconstructing the invariant sets from multisite neural recordings. Moreover, we found that this approach could be used to distinguish among the various types of CFC (Hyafil et al., 2015b) (phase-amplitude, phase-phase, phase-frequency, amplitude-amplitude, etc) which is another fundamental issue confounding the traditional CFC algorithms (data not shown) (Hyafil, 2015). However, robustness of this approach in noisy experimental data remains to be tested.

It is essential to note that the approach based on the analysis of the multidimensional invariant sets to characterize the PAC patterns remains valid irrespective of the particular limitations of a given network model. For example, the SH bifurcation can lead to a intermittent PAC pattern via the saddle-node on invariant circle bifurcation (SNIC) (Fontolan et al., 2013). In particular, the switching between the continuous and the intermittent PAC patterns through the SNIC bifurcation has been analyzed from stochastic neural network models with dynamic synapses (binary-state discrete-time neuron model) (Sase et al., 2017), using a particular network architecture equivalent to that shown in Fig. 12a. Moreover, torus canard is a dynamic phenomenon capable of generating PAC by separating the regimes of spiking and bursting in neural activity and it is commonly observed in generic slow-fast dynamical systems (i.e. coexistence of multiple time scales) (Benes et al., 2011; Krupa et al., 2012; Mitry et al., 2013; Burke et al., 2012).

5.1. PAC as biomarker of Parkinson's disease

Our main motivation to develop the tools involved in this work was to study the underlying mechanisms of the PAC phenomenon in the context of PD. The identification and study of biomarkers of PD are relevant tasks for understanding the pathophysiology and progression of the disease, as well as for improvement of early clinical diagnosis and treatments. In particular, $\beta - \gamma$ PAC observed in the primary motor cortex of patients is exaggerated in the parkinsonian state and may be related to motor dysfunction in PD (de Hemptinne et al., 2013, 2015). Moreover, evidence exist showing a correlation between PAC intensity and severity of motor symptoms in PD patients (van Wijk et al., 2016; Tsiokos et al., 2017) and a monkey model of parkinsonism (Sanders et al., 2013). This evidence supports the hypothesis that PAC is a biomarker of the parkinsonian state that could improve the DBS therapy by using it as a feedback signal to develop closed-loop DBS devices capable to deliver adaptive stimulation patterns (de Hemptinne et al., 2015; Gunduz et al., 2015).

In spite of this evidence supporting the relevance of PAC in PD, the interpretation and functional significance of the observed PAC patterns an important open issues in this context. One hypothesis is that the overcoupling between independent frequency bands ("true" $\beta - \gamma$ nonharmonic PAC) impairs information flow in the BG-thalamocortical network causing motor dysfunction (de Hemptinne et al., 2013; Alhourani et al., 2016). On the other hand, the observed PAC might be a trivial epiphenomenon related to the nonsinusoidal waveform shape produced by a single nonlinear oscillator in the β band (Cole et al., 2017), that is, "spurious" harmonic PAC elicited by harmonically related spectral components.

In this context, we analyzed the underlying mechanisms of PAC using the Wilson-Cowan model shown in Fig. 2, which represents the interaction of the cortex (N_1) with the BG network (N_2–N_3). More specifically, the proposed model is a functional representation of the main loops conforming the BG-thalamocortical network: direct (N_1–N_1), hyperdirect (N_1–N_2) and indirect (N_1–N_3–N_2) loops. In the proposed model, the competition between the loops was explored by varying the synaptic efficacy G_{ij} of the connections. Figs. 6 and 8 show the phase space corresponding to the competition between the hyperdirect (G_{12}) and indirect (G_{13}) loops while the direct loop was kept unchanged (G_{11} constant). We found that the competition between the hyperdirect and the direct loops generates slow oscillations (4 Hz) via a Hopf bifurcation. In line with the results of Leblois et al. (2006) and Velarde et al. (2017), this dynamics can be interpreted as pathological oscillations in the parkinsonian state. On the other hand, the synaptic efficacy G_{13} in the indirect loop favors the formation of fast oscillations (50 Hz) in the BG network (N_2–N_3), either by activation of the node N_3 or by a Hopf bifurcation. These results are consistent with the experimental observations presented in West et al. (2018); de Hemptinne et al. (2013) regarding the origin of oscillations in the BG-thalamocortical network. In Ref. West et al. (2018), using directed connectivity analysis in the BG-thalamocortical circuit, the authors propose the following mechanisms: I) Long-loop resonance: pathological β arises from induction of a loop formed by feedback between cortex and BG. This mechanisms implies that the dopamine-depleted state is associated with a strengthening of the hyperdirect loop and subthalamo-cortical feedbacks. II) Subcortical generator: γ oscillations arises from subcortical interactions and local dynamics within BG network. This would imply that external globus pallidus and striatum are necessary structures for the propagation of γ interactions.

In our model, the motor cortex (N_1) acts as a slow oscillator projecting, via the indirect loop, over a fast oscillator given by the BG network (N_2–N_3). This architecture gives rise to the emergence of "true" nonharmonic PAC via the SH bifurcation (Fig. 9) or the PEI mechanism (arrow d in Fig. 6), depending on the gain of the hyperdirect (G_{12}) and indirect (G_{23}) loops. The role of the direct loop is also relevant in order to account for possible effects of dopamine depletion (Leblois et al., 2006; Velarde et al., 2017). Therefore, in Appendix E we analyzed the effect of the change in the gain of the direct loop (G_{11}). We found that the PAC intensity, as measured by the PLV metric, is sightly reduced as the G_{11} is increased. This behavior was observed for the two nonharmonic PAC mechanisms: the SH bifurcation (Left graphs in Figs. 20 and 21) and PEI mechanism (Right graph in Fig. 20). Preliminarily, these results are compatible with the hypothesis suggesting that exaggerated PAC emerges in the parkinsonian state under dopamine depletion de Hemptinne et al. (2013).

It is worth noting that the exact frequency of the oscillations can be changed, irrespective of the underlying mechanisms, by tuning the time constants and delays of the connections (Eq. (2) and Table 1). More important, the results described above show that the pathological slow oscillations (e.g. β band) and the "true" nonharmonic PAC emerge from dissimilar underlying mechanisms and are associated to the competition of different BG-thalamocortical loops. This observation supports the relevance of PAC as a biomarker of PD, suggesting that it is not an

epiphenomenon related to the pathological β band oscillations.

6. Conclusion

In this work, we study and characterize PAC patterns emerging from several basic architectures previously identified as biologically plausible neuronal circuits for the generation of nested frequency patterns. In addition, we investigate the emergence of PAC in a model of BG-thalamocortical network associated with PD.

We found that two PAC classes can coexist in the dynamics of the analyzed networks: 1) harmonic PAC which is an epiphenomenon of the nonsinusoidal waveform shape, and 2) nonharmonic PAC associated with true coupled oscillatory dynamics with independent frequencies elicited by a secondary Hopf bifurcation and mechanisms involving periodic excitation/inhibition of a network population. The analysis we propose, based on bifurcation theory and the topological properties of the invariant sets, allows the identification of the underlying mechanisms of different oscillatory dynamics that have been experimentally observed in a variety of neural architectures, which challenge and confound traditional signal processing algorithms aimed to assess PAC.

Finally, we use the proposed tools to study the functional significance of the PAC phenomenon in the context of PD. Our results provide theoretical arguments that demonstrate that nonharmonic PAC is not an epiphenomenon related to the pathological β band oscillations, thus supporting the experimental evidence about the relevance of PAC as a potential biomarker of PD.

7. Competing interests

The authors declare that they have no significant competing financial, professional, or personal interests that might have influenced the performance or presentation of the work described in this manuscript.

Appendix A. Biologically plausible neural networks.

Fig. 12 shows four types of biologically plausible neural networks analyzed in Hyafil et al. (2015b). Architecture a) (Fig. 12a) corresponds to the case where the slow oscillation (SO) is not internally generated but introduced by an oscillatory input which modulates the intrinsic fast oscillation (FO) produced by the network. The modulatory effect of the external oscillatory input elicits the PAC pattern observed in architecture a). Architectures b), c), d) and e) are independent CFC networks, that is, they do not require oscillatory input to produce CFC. In these architectures, distinct populations are implicated in the generation of the SO and the FO. In architectures b) and c), two oscillatory populations are unidirectionally and reciprocally coupled, respectively (Fig. 12b and c). Architecture d) is a intermingled network where the circuits generating individual oscillations share a common subpopulation (Fig. 12d). In architecture b), PAC arises due to the modulatory effect of the efferent population onto the rhythm produced by the afferent population. A more complex dynamics was found in architectures c) and d) in which the PAC patterns are elicited by specific bifurcation structures emerging from the system dynamics, besides the modulatory effect of one oscillatory population onto the rhythm produced by another modulated population.

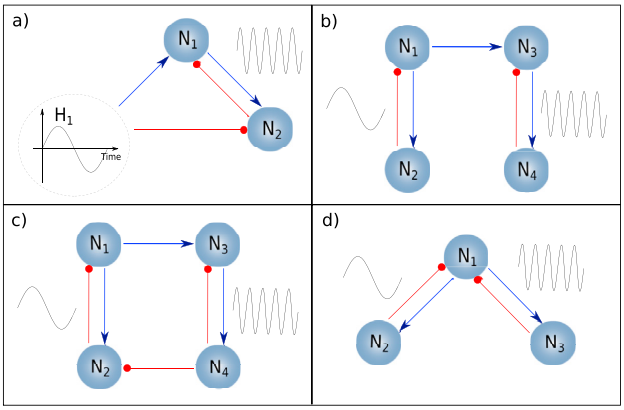

Fig. 12. Biologically plausible networks for emerging cross-frequency neural coupling: a) Sensory entrainment. b) Unidirectional coupling. c) Bidirectional coupling. d) Intertwined oscillators.

In the following subsections, we will show the results associated with each architecture. All the parameters for networks are summarized in Table 2.

Table 2
Values of the coupling parameters, time constants and delays for networks a) to d).

	Synaptic efficacy	Delay	Time constant
	G	Δ (ms)	τ_{act} (ms)
Architecture a)			
$1 \to 2$	1.4	5	0.1
$2 \to 1$	-1	5	0.1
Architecture b)			
$1 \to 2$	(0,3)	35	40
$2 \to 1$	-1	35	40
$3 \to 4$	(0,2)	5	0.1
$4 \to 3$	-1	5	0.1
$1 \to 3$	1	5	20

(*continued on next column*)

Table 2 (*continued*)

	Synaptic efficacy	Delay	Time constant
	G	Δ (ms)	τ_{acf} (ms)
Architecture c)			
$1 \to 2$	2.5	35	40
$2 \to 1$	-1	35	40
$3 \to 4$	1.4	5	10
$4 \to 3$	-1	5	10
$1 \to 3$	(0,2)	5	20
$4 \to 2$	(-2,0)	5	20
Architecture d)			
$1 \to 2$	(0,6)	35	40
$2 \to 1$	-1	35	40
$1 \to 3$	(0,2)	5	0.1
$3 \to 1$	-1	5	0.1

Notation (x,y) indicates $x \leq G_{ij} \leq y$. The values of inputs H_i are specified in Appendix.

Sensory entrainment: Oscillator with time-dependent external inputs

Consider an oscillator with period $\frac{1}{\omega_1}$ and composed of two nodes where the external inputs are $H_i = h_i \cos(\omega_2 t + \phi_i) + d_i$ $(i = 1, 2)$ (see Fig. 12a). Here the frequency ω_1 can be determined using the characteristic equation $p(2\pi i\omega_1) = 0$, where

$$p(\lambda) = (1 + \lambda\tau_1)(1 + \lambda\tau_2) - G\exp(-\lambda\Delta) = 0$$

$$\Rightarrow \begin{cases} \tan(2\omega_1\Delta) & = \dfrac{-2\omega_1\tau}{1 - (\omega_1\tau)^2}, \\ |G| & = 1 + (\omega_1\tau)^2 \end{cases} \tag{A1}$$

and $G = G_{12}G_{21}$ is the parameter that controls the Hopf bifurcation. Based on the linear analysis of the system and using the conditions of activation of nodes ($\alpha_i > 0$), we determine two regions in the constant input space (H_1, H_2) (see Fig. 13): (R_1) both active nodes, (R_2) at least one node inactive. In region R_1, an oscillatory dynamics with characteristic frequency ω_1 is generated and this corresponds to the linear regime of the system.

On the other hand, the oscillatory external stimulations of the system describe an ellipse $\vec{H}(t)$ in the space (H_1, H_2). The parameters ϕ_i, h_i and d_i determine the center, angle of rotation and axis of the ellipse (see Fig. 13).

Different scenarios may exist depending on the geometrical characteristics of $\vec{H}(t)$. First, if the ellipse is totally contained in (R_1), there is a coexistence of oscillations ω_1 and ω_2 during the entire cycle of the ellipse (Fig. 13a). The other limit is when the ellipse does not intersect with region R_1 (Fig. 13b). In this case, the external inputs do not affect the system dynamics which oscillates at a single frequency ω_2.

The intermediate situation is when there is only one part of the cycle with a superposition of oscillations (Fig. 13c). This scenario gives rise to intermittent PAC through the PEI mechanism. The mathematical condition for this situation can be derived from the intersection between the ellipse and a straight line (condition of activation):

$$h_1^2 + (A.h_2)^2 - 2A.h_1.h_2\cos(\phi) \geq (d_1 - A.d_2)^2. \tag{A2}$$

where A is the slope of the straight line. In Fig. 13, A is a combination of G_{12} and G_{21} that defines the border of R_1.

In conclusion, if the architecture presented in Fig. 12a is configured with parameters that verify the conditions A1 and A2, then the system gives rise to intermittent PAC through the PEI mechanism. These conditions are valid in the adiabatic limit $\omega_2 << \omega_1$, although in practice they are roughly valid whenever a mild temporal scale separability is present.

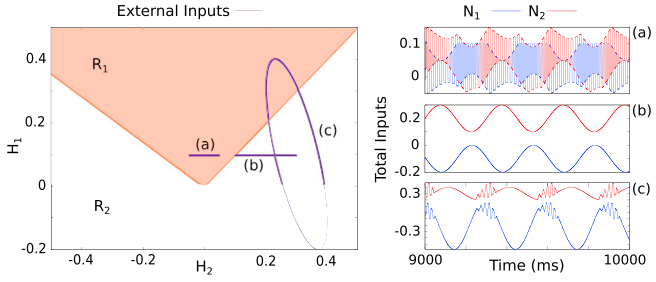

Fig. 13. Results corresponding to the architecture of Fig. 12a. States of the system presented in Fig. 12a as function of external inputs. R_1 is the region where both nodes are active. (a) External inputs are enough to active both nodes, then two frequencies coexist ($\omega_1 = 50$ Hz, $\omega_2 = 4$ Hz). (b) When some node is inactive, then there is only one oscillatory component $\omega_2 = 4$ Hz. (c) Intermittent PAC is generated by partial intersection of ellipse (H_1, H_2) with R_1. The configuration of the network is presented in Table 2.2

Unidirectional coupling

Consider a network composed of four interconnected nodes as shown in Fig. 12b. Note that this is equivalent to two oscillators N_1–N_2 and N_3–N_4, where the second receives the output of the first one. The dynamics can be expressed by the equations

$$\begin{cases} (\dot{m}_{12}, \dot{m}_{21}) = F(m_{12}, m_{21}, H_1(t)) \\ (\dot{m}_{34}, \dot{m}_{43}) = F(m_{34}, m_{43}, G_{13} m_{13}(t - \Delta_{13})) \\ \tau_{13} \dot{m}_{13} = -m_{13} + A_1 \end{cases} \tag{A3}$$

where the function F denotes the dynamics of a unique oscillator (see Eq. (A1)).

The external input to the system H_1 is not oscillatory. When the subsystem N_1–N_2 is active, it is responsible for generating and sending an oscillatory signal (with frequency ω_2) to subsystem N_3–N_4 that is oscillating with frequency ω_1. Therefore, it is equivalent to case 'Sensory entrainment'. Furthermore, the input of subsystem N_3–N_4 is always positive and has the frequency of subsystem N_1–N_2.

The connection between nodes 1 and 3 represents the transmission of oscillations with frequency ω_2. Using the Fourier transform, the spectral component received by subsystem N_3–N_4 can be calculated

$$|H_3(\omega_2)| = \frac{G_{13}}{\sqrt{1 + (\omega_2 \tau_{13})^2}} |A_1(\omega_2)|. \tag{A4}$$

In this work, we consider $G_{13} = 1$, $\tau_{13} = 20$ ms obtaining $|H_3| \approx 0.99|A_1|$. In Fig. 14, we plot the PLV as a function of (G_{12}, G_{34}) (left panel). When either of the two subsystems is not in an oscillatory state, the PLV is zero. In Fig. 14 right, we show the signal I_3 with intermittent PAC (top) generated by the oscillator N_3–N_4 with oscillatory external input $H_3 = G_{13} m_{13}$ (i.e. PEI mechanism). This external input is marked with the solid vertical line in (H_4, H_3)-plane (bottom) and it is contained in the region where the subsystem N_3–N_4 is active (shaded area). These results correspond to the configuration $G_{12} = 2.5$, $G_{34} = 1.5$ and $H_1 = 0.01$.

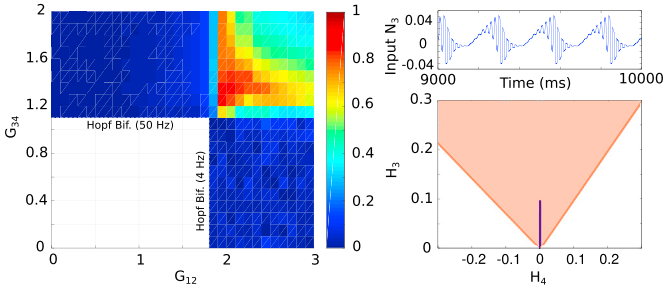

Fig. 14. Results corresponding to the architecture of Fig. 12b. (Left) PLV as function of (G_{12}, G_{34}). There are two independent Hopf bifurcations, $G_{12} \approx 1.8$ and $G_{34} \approx 1.1$. (Right Top) Total input in node 3. As in the architecture 'Sensory entrainment', the intermittent PAC in the subnetwork N_3–N_4 emerges as consequence the input proportional to the oscillatory signal m_{13} generated by N_1–N_2. (Right Bottom) $H_3 = G_{13} m_{13}$ is marked with the solid vertical line in (H_4,H_3)-plane. The shaded region corresponds to where the subsystem N_3–N_4 is active. In this case, the configuration is $G_{12} = 2.5$ and $G_{34} = 1.5$.

Bidirectional coupling

Consider a network composed of two interconnected oscillators as shown in Fig. 12c. We analyzed the competition between connections G_{13} and G_{42} as a mechanism of generation of PAC.

First, when $G_{42} \to 0$, the dynamics corresponds to the unidirectional coupling described in the previous section (Fig. 12b). When $G_{13} \to 0$, the oscillator N_1–N_2 is stimulated by a high frequency oscillation ($\omega_1 > \omega_2$) with negative polarity ($G_{42} < 0$). In this situation, the network has three possible states: 1) inactive system, 2) synchronization with frequency ω_1, 3) coexistence of two frequencies.

In Fig. 15, the PLV is shown as a function of the efficacy G_{42}. Note that the curve of the PLV as a function of G_{42} is shifted, with little changes in its shape, as the synaptic efficacy G_{13} is varied. The index was calculated for I_2 (top) and I_3 (bottom). For each node, the input signal was plotted in three cases (right panel): $G_{42} < -0.5$ (top), $G_{42} = -0.5$ (center), $G_{42} > -0.5$ (bottom). It is worth noting that the waveform shape of the PAC patterns and the PLV values obtained in nodes 2 and 3 are different. These results correspond to the configuration presented in Table 2 and $H_1 = 0.1$.

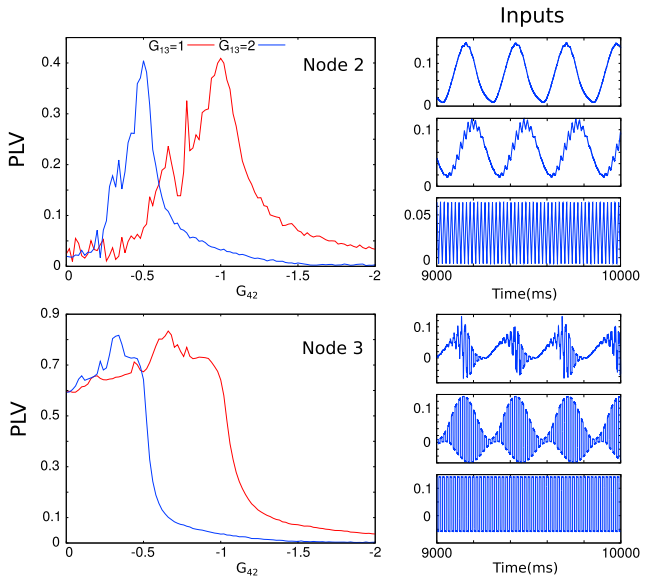

Fig. 15. Results corresponding to the architecture of Fig. 12c. (Left) PLV in nodes 2 and 3 as a function of G_{42} for two values of G_{13}. (Right) There are three characteristic points. 1) When $G_{42} \to 0$, there is only transmission of information from slow oscillator (N_1–N_2) to fast oscillator (N_3–N_4). Activity of node 2 is 4 Hz oscillation; while in node 3, intermittent PAC emerges(see the top boxes of node 2 and 3). 2) The competition between gains causes PAC. The phase of slow oscillator determines if node 3 is active or not. When node 3 generates 50 Hz oscillation, intermittent PAC in node 2 is observed (see middle boxes of node 2 and 3). 3) For sufficiently large values of G_{42}, the fast oscillator manages to synchronize the system dynamics (see bottom boxes of node 2 and 3).

Intermingled network

Consider three nodes interconnected as shown in Fig. 12d. In this case, the oscillators share a common population. We represented the variation of PLV in the space (G_{12}, G_{13}) in the color map shown in Fig. 16. We observed the existence of two independent Hopf bifurcations, whose boundaries are indicated with dashed lines in the map. The intersection of the boundaries define a double Hopf point where two frequencies coexist. Given that the BG-thalamocortical network presented in Fig. 2 is composed by a intermingled network, this bifurcation structure is similar to the one shown in Fig. 8. In Fig. 16, the high PLV values observed after the HH bifurcation are produced by a nonsinusoidal slow oscillation ("spurious" harmonic PAC). In this network, the SH bifurcations occurring nearby the HH bifurcations elicit "true" nonharmonic PAC similarly to what was observed in Fig. 9 (right) and 17 (right) for the configuration B of the network shown in Fig. 2. These results correspond to the configuration presented in Table 1–2 and $H_1 = 0.1$.

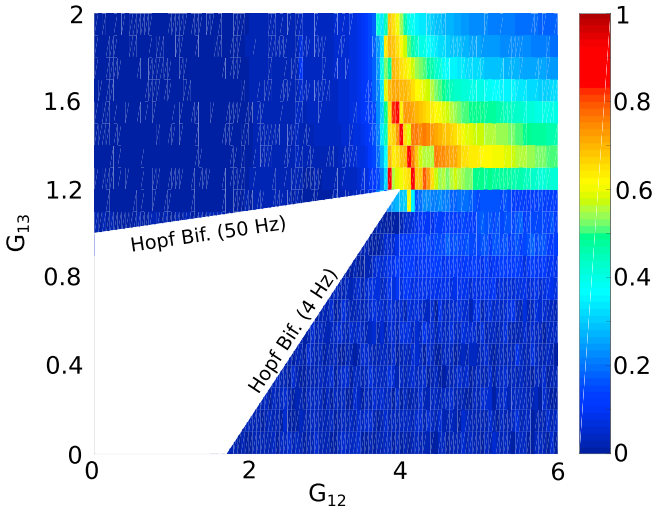

Fig. 16. Results corresponding to the architecture of Fig. 12d. PLV as function of (G_{12}, G_{13}). The dashed white lines indicate the Hopf bifurcations.

Appendix B. Modulation Index

The Modulation Index based on the Kullback-Leibler distance (KLMI) is a previously reported nonparametric PAC metrics aimed to assess phase-amplitude cross frequency coupling between two frequency bands of interest (Tort et al., 2008, 2009, 2010). Following Tort et al. (2010), we show here the steps required for the computation of the KLMI.

The existence of phase-amplitude coupling is characterized by a deviation of the amplitude distribution P from uniformity in a phase-amplitude histogram. This was achieved by an adaptation of the KullbackLeibler (KL) distance, a metric that is widely used in statistics and in information

theory to quantify the difference between two distributions (Kullback and Leibler, 1951).

KLMI is defined as

$$\mathrm{KLMI} = \frac{D_{KL}(P,U)}{\log(N)} = 1 + \frac{\sum_{j=1}^{N} P(j)\log(P(j))}{\log N} \tag{B1}$$

where U is the uniform distribution. Let us notice that $\log N$ is the maximal possible value of the entropy, corresponding to the uniform distribution. For that reason, the KLMI is defined by dividing the KL distance of the observed amplitude distribution from the uniform distribution by $\log N$.

Therefore if the mean amplitude of the high frequency signal is uniformly distributed over the phases of the low frequency signal, we have KLMI ≈0; KLMI increases as P deviates from U corresponding to a higher KL distance.

Fig. 17 shows the KLMI as function of parameters G_{12} and G_{13} corresponding to the phase space of the BG-thalamocortical network (Fig. 2) for both configurations A and B.

Let us note that although PLV and KLMI metrics are both aimed to assess PAC, yet they measure different characteristics of the processed time series. Specifically, the PLV quantifies the degree of phase synchronization between the slow oscillation and the amplitude envelope of the fast oscillation (Eqs. (17) and (18)). On the other hand, the KLMI quantifies the non-uniformity distribution of the fast oscillation amplitudes over the phase bins of the slow oscillation (Eq. (B1)). As a consequence, differences are observed when these PAC metrics are used to characterize the same dynamics, which is illustrated in Figs. 9 and 17 for the dynamics of the network shown in Fig. 2. Although both metrics correctly report significant PAC intensity above the SH bifurcations where "true" nonharmonic PAC exists, they also indicate high PAC intensity in phase space regions characterized by nonsinusoidal slow oscillations with no CFC ("spurious" harmonic PAC): ($0.5 < G_{12} < 2$ and $0 < G_{13} < 0.5$) in Fig. 7 left for PLV and ($1 < G_{12} < 3$ and $0 < G_{13} < 2$) in Fig. 17 right for KLMI. Importantly, the presence of the harmonically related spectral components in these two regions of the phase space is revealed by the TLI metric as shown in Fig. 10. It is worth noting that, the differences between the results obtained with the PLV and KLMI metrics also depends on the bandwidth of the band-pass filters used to extract the slow and fast rhythms.

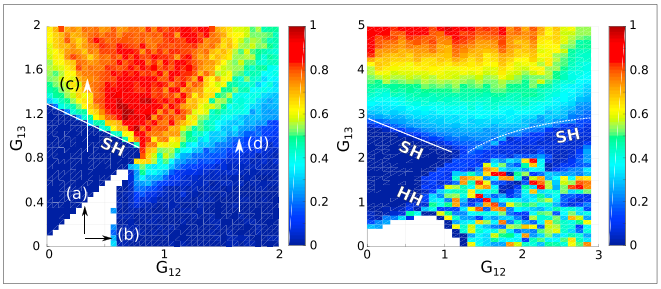

Fig. 17. Normalized Modulation Index (KLMI) as a function of the synaptic efficacies (G_{12}, G_{13}). Left and right panels correspond to configurations A and B of BG-thalamocortical network (Fig. 2), respectively. Dashed lines mark secondary Hopf bifurcation (SH). Arrow (a) and (b) indicate the formation of limit cycle via activation or Hopf bifurcation, respectively. Arrows (c) and (d) show discontinuous and continuous variations of KLMI, respectively. In both cases, KLMI was computed for the signal I_3. Compare with Fig. 9.6

Appendix C. Applications of TLI in the Van der Pol oscillator.

Any non-linear oscillator can be used as a model that generates spurious PAC via separation of time scales due to nonlinear effects. As example, we consider a Van der Pol oscillator whose equation is given by

$$\ddot{x} - \mu\left(1 - x^2\right)\dot{x} + \omega^2 x = 0 \tag{C1}$$

where μ is a scalar parameter controlling the nonlinearity and $\omega = 2\pi f$ is the angular frequency of oscillation when $\mu = 0$. We fixed $f = 10$ Hz. Fig. 18 shows the indexes characterizing the cross-frequency coupling in the Van der Pol oscillator as functions of $\frac{\mu}{\omega}$.

For the evaluation of the indexes, the band-pass filters were configured with a null-to-null bandwidth of 1–15 Hz (to obtain x_{LF}) and 20–100 Hz (to obtain x_{HF}). The former includes the fundamental frequency of the oscillator for all the explored of the parameter μ, and the latter contains several harmonics of the fundamental frequency. Besides, additive white Gaussian noise was added to the dynamics obtained from the oscillator prior to compute the PLV, KLMI and TLI metrics.

It is essential to note that, though the TLI metric is bounded in the range [0,1] and it is robust against variations of the bandwidth of the band-pass filters used to extract x_{LF} and x_{HF} time series, the absolute minimum TLI value obtained in absence of harmonic oscillations does depend on the noise level of the processed signal and on the epoch length, i.e. the number of periods of the low-frequency oscillation taken to implement the time-locked average. Therefore, the key point indicating the presence of harmonic PAC is given by the concurrent increasing of the TLI with PAC metrics (PLV and KLMI) as the parameter μ is increased as it is shown in Fig. 18, rather than by the absolute TLI value. From the insets of Fig. 18 it is clear the presence of harmonics associated to the nonsinusoidal waveform shapes as a consequence of the nonlinear effects (μ). It is worth noting that the nonsinusoidal waveform shapes produced by the Van der Pol oscillator give rise to bimodal phase distribution with two local maxima in opposite phase angles. Accordingly, we compute the PLV using Eq. (17) with $\Delta\phi = 2\phi(x_{LF}) - \phi(A(x_{HF}))$. For a detailed discussion about the performance of the PLV and KLMI metrics in the case of multimodal phase distribution the reader is referred to Tort et al. (2010) and Cohen (2014) (Sec. 19.8, p. 257).

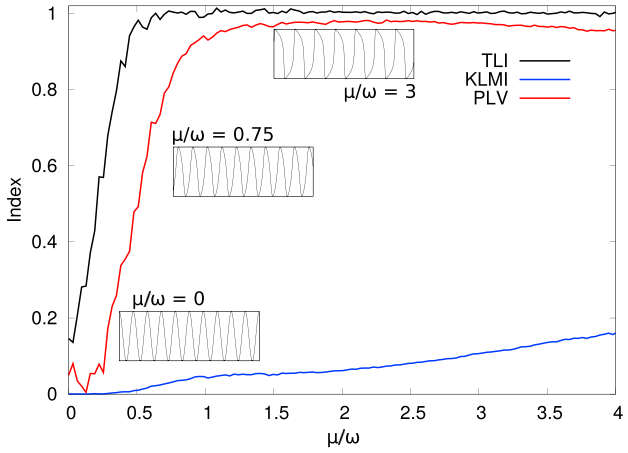

Fig. 18. Characterization of cross-frequency coupling in the Van der Pol oscillator. PLV, KLMI and TLI as function of $\frac{\mu}{\omega}$. All indexes increase concurrently. This shows that we are observing harmonic PAC. In the inset plots, the solution of Eq. (C1) for three values of μ is shown.7

Appendix D. Dynamics of BG-thalamocortical network.

In Fig. 19, we plot the temporal evolution of I_j ($j = 1, 2, 3$) in the different dynamical states of the BG-thalamocortical network. Each column is associated with a node, while each row corresponds to a dynamical state. From top to bottom, we show: 1) Slow oscillation as a consequence of the Hopf bifurcation (see Fig. 6b). 2) Fast oscillation as a consequence of the activation of node 3 (see Fig. 6a). 3) Secondary Hopf bifurcation (see Fig. 6c). 4) Mechanism of periodic excitation/inhibition (see Fig. 6d). 5) Hopf-Hopf bifurcation (see Fig. 8c).

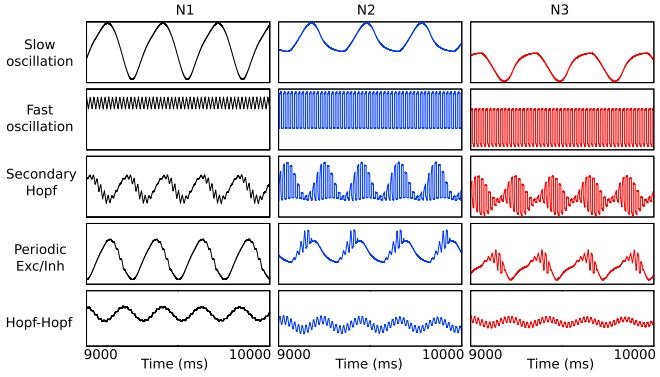

Fig. 19. Temporal evolution of inputs I_j for each node and different dynamical states corresponding to the BG-thalamocortical network shown in Fig. 2.8

Appendix E. Effect of the direct loop in the dynamics of BG-thalamocortical network.

In Figs. 20 and 21, we plot PLV as function of G_{11} (direct loop) and G_{13} (indirect loop) in configuration A and B, respectively. Each figure shows two situations: left panel) $G_{12} = 0.5$. right panel) $G_{12} = 1.5$.

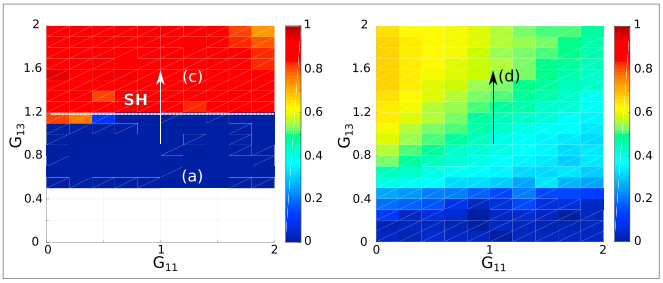

Fig. 20. Effect of G_{11}. Absolute value of PLV as a function of the synaptic efficacies (G_{11}, G_{13}) in configuration A of BG-thalamocortical network. Left) For $G_{12} = 0.5$, PLV is independent to G_{11} Right) For $G_{12} = 1.5$, PLV depends of G_{11}, however, the bifurcation structure does not change. Compare with Fig. 9 left.9

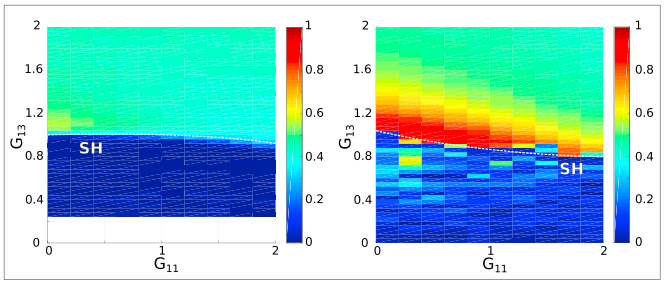

Fig. 21. Effect of G_{11}. Absolute value of PLV as a function of the synaptic efficacies (G_{11}, G_{13}) in configuration B of BG-thalamocortical network. Left) For $G_{12} = 0.5$, PLV is independent to G_{11} Right) For $G_{12} = 1.5$, PLV depends on G_{11}, however, the bifurcation structure does not change. Compare with Fig. 9 right.10

In the case $G_{12} = 0.5$ (left panel in Figs. 20 and 21), G_{11} does not significantly modify the curves of the SH bifurcation and activation of node 3 (see arrows (a), (c) and SH in Fig. 9). When $G_{12} = 1.5$ (right panel in Figs. 20 and 21), PLV is a decreasing function of G_{11}, however the structure of the bifurcations is not modified (see arrows (d) and SH in Fig. 9).

As we emphasize in the Discussion section, the slow oscillations are generated as a consequence of the competition between direct ($G_d = G_{11}$) and hyperdirect (G_h) loops, while the fast oscillations emerge from the N_2–N_3 interaction. In the first case ($G_{12} = 0.5$), the system cannot generate slow oscillations via a Hopf bifurcation and the dynamics of the fast oscillations is independent of G_{11}. In the second case ($G_{12} = 1.5$), the system generates slow oscillations via Hopf bifurcation and its interaction with the fast oscillations (reflected in the PLV) will depend on the value of G_{11} although it does not modify the structure of the discussed mechanisms.

Appendix F. Supplementary data

Supplementary data to this article can be found online at https://doi.org/10.1016/j.neuroimage.2019.116031.

References

Walker, J.J., Terry, J.R., Lightman, S.L., 2010. Origin of ultradian pulsatility in the hypothalamic–pituitary–adrenal axis. Proc. R. Soc. Biol. Sci. 277 (1688), 1627–1633. https://doi.org/10.1098/rspb.2009.2148. https://royalsocietypublishing.org/doi/abs/10.1098/rspb.2009.2148.

Ahnaou, A., Huysmans, H., Biermans, R., Manyakov, N.V., Drinkenburg, W.H.I.M., 2017. Ketamine: differential neurophysiological dynamics in functional networks in the rat brain. Transl. Psychiatry 7 (9), e1237, 09.

Albin, R.L., Young, A.B., Penney, J.B., Oct 1989. The functional anatomy of basal ganglia disorders. Trends Neurosci. 12 (10), 366–375.

Alhourani, A., Crammond, D.J., Kondylis, E.D., Randazzo, M.J., Wozny, T.A., Lipski, W.J., Pandya, Y., Ghuman, A.S., Richardson, R.M., Turner, R.S., 2016. Movement-related dynamics of cortical oscillations in Parkinsons disease and essential tremor, 06 Brain 139 (8), 2211–2223. https://doi.org/10.1093/brain/aww144. ISSN 0006-8950. https://dx.doi.org/10.1093/brain/aww144.

Amiri, M., Frauscher, B., Gotman, J., 2016. Phase-amplitude coupling is elevated in deep sleep and in the onset zone of focal epileptic seizures. Front. Hum. Neurosci. 10, 387. https://doi.org/10.3389/fnhum.2016.00387. ISSN 1662-5161. https://www.frontiersin.org/article/10.3389/fnhum.2016.00387.

Aru, J., Aru, J., Priesemann, V., Wibral, M., Lana, L., Pipa, G., Singer, W., Vicente, R., 2015. Untangling cross-frequency coupling in neuroscience. Curr. Opin. Neurobiol. 31, 51–61. ISSN 0959-4388. https://doi.org/10.1016/j.conb.2014.08.002. http://www.sciencedirect.com/science/article/pii/S0959438814001640. SI: Brain rhythms and dynamic coordination.

Aydore, S., Pantazis, D., Leahy, R.M., 2013. A note on the phase locking value and its properties. Neuroimage 74, 231–244. ISSN 1053-8119. https://doi.org/10.1016/j.neuroimage.2013.02.008. http://www.sciencedirect.com/science/article/pii/S1053811913001286.

Benes, G.N., Barry, A.M., Kaper, T.J., Kramer, M.A., Burke, J., 2011. An elementary model of torus canards. Chaos: An Interdisciplinary Journal of Nonlinear Science 21 (2), 023131. https://doi.org/10.1063/1.3592798. https://doi.org/10.1063/1.3592798.

Bergmann, T.O., Born, J., Jan 2018. Phase-amplitude coupling: a general mechanism for memory processing and synaptic plasticity? Neuron 97 (1), 10–13.

Bragin, A., Jando, G., Nadasdy, Z., Hetke, J., Wise, K., Buzsaki, G., Jan 1995. Gamma (40-100 Hz) oscillation in the hippocampus of the behaving rat. J. Neurosci. 15 (1 Pt 1), 47–60.

Burke, J., Desroches, M., Barry, A.M., Kaper, T.J., Kramer, M.A., Feb 2012. A showcase of torus canards in neuronal bursters. J. Math. Neurosci. 2 (1), 3. https://doi.org/10.1186/2190-8567-2-3. ISSN 2190-8567. https://doi.org/10.1186/2190-8567-2-3.

Canolty, R.T., Knight, R.T., 2010. The functional role of cross-frequency coupling. Trends Cogn. Sci. 14 (11), 506–515. ISSN 1364-6613. https://doi.org/10.1016/j.tics.2010.09.001. http://www.sciencedirect.com/science/article/pii/S1364661310002068.

Canolty, R.T., Edwards, E., Dalal, S.S., Soltani, M., Nagarajan, S.S., Kirsch, H.E., Berger, M.S., Barbaro, N.M., Knight, R.T., 2006. High gamma power is phase-locked to theta oscillations in human neocortex. Science 313 (5793), 1626–1628. https://doi.org/10.1126/science.1128115. ISSN 0036-8075. http://science.sciencemag.org/content/313/5793/1626.

Cohen, M.X., 2014. Analyzing Neural Time Series Data : Theory and Practice. MIT Press.

Cole, S.R., Voytek, B., 2017. Brain oscillations and the importance of waveform shape. Trends Cogn. Sci. (Regul. Ed.) 21 (2), 137–149, 02.

Cole, S.R., van der Meij, R., Peterson, E.J., de Hemptinne, C., Starr, P.A., Voytek, B., 2017. Nonsinusoidal beta oscillations reflect cortical pathophysiology in Parkinson's disease. J. Neurosci. 37 (18), 4830–4840. https://doi.org/10.1523/JNEUROSCI.2208-16.2017. ISSN 0270-6474. http://www.jneurosci.org/content/37/18/4830.

Connolly, A.T., Jensen, A.L., Bello, E.M., Netoff, T.I., Baker, K.B., Johnson, M.D., Vitek, J.L., 2015. Modulations in oscillatory frequency and coupling in globus pallidus with increasing parkinsonian severity. J. Neurosci. 35 (15), 6231–6240. https://doi.org/10.1523/JNEUROSCI.4137-14.2015. ISSN 0270-6474. http://www.jneurosci.org/content/35/15/6231.

de Hemptinne, C., Ryapolova-Webb, E.S., Air, E.L., Garcia, P.A., Miller, K.J., Ojemann, J.G., Ostrem, J.L., Galifianakis, N.B., Starr, P.A., 2013. Exaggerated phase–amplitude coupling in the primary motor cortex in Parkinson disease. Proc. Natl. Acad. Sci. 110 (12), 4780–4785. https://doi.org/10.1073/pnas.1214546110. ISSN 0027-8424. https://www.pnas.org/content/110/12/4780.

de Hemptinne, C., Swann, N.C., Ostrem, J.L., Ryapolova-Webb, E.S., San Luciano, M., Galifianakis, N.B., Starr, P.A., May 2015. Therapeutic deep brain stimulation reduces cortical phase-amplitude coupling in Parkinson's disease. Nat. Neurosci. 18 (5), 779–786.

Dellavale, D., Rosselló, J.M., 2019. Cross-frequency couplings in non-sinusoidal dynamics of interacting oscillators: acoustic estimation of the radial position and spatial stability of nonlinear oscillating bubbles. Ultrason. Sonochem. 51, 424–438. ISSN 1350-4177. https://doi.org/10.1016/j.ultsonch.2018.07.026. http://www.sciencedirect.com/science/article/pii/S1350417718302529.

DeLong, M.R., Jul 1990. Primate models of movement disorders of basal ganglia origin. Trends Neurosci. 13 (7), 281–285.

Dietrich, J.W., Landgrafe, G., Fotiadou, E.H., 2012. TSH and thyrotropic agonists: key actors in thyroid homeostasis. J. Thyroid Res. 2012, 351864.

Dvorak, D., Fenton, A.A., 2014. Toward a proper estimation of phaseamplitude coupling in neural oscillations. J. Neurosci. Methods 225, 42–56. ISSN 0165-0270. https://doi.org/10.1016/j.jneumeth.2014.01.002. http://www.sciencedirect.com/science/article/pii/S0165027014000132.

Eswaraiah, S., Kim, Y.H., Lee, J., Ratnam, M.V., Rao, S.V.B., 2018. Effect of southern hemisphere sudden stratospheric warmings on Antarctica mesospheric tides: first observational study. J. Geophys. Res.: Space Physics 123 (3), 2127–2140. https://doi.org/10.1002/2017JA024839. https://agupubs.onlinelibrary.wiley.com/doi/abs/10.1002/2017JA024839.

Fell, J., Axmacher, N., Feb 2011. The role of phase synchronization in memory processes. Nat. Rev. Neurosci. 12 (2), 105–118.

Fontolan, L., Krupa, M., Hyafil, A., Gutkin, B., Aug 2013. Analytical insights on theta-gamma coupled neural oscillators. J. Math. Neurosci. 3 (1), 16. https://doi.org/10.1186/2190-8567-3-16. ISSN 2190-8567. https://doi.org/10.1186/2190-8567-3-16.

Fries, P., 2005. A mechanism for cognitive dynamics: neuronal communication through neuronal coherence. Trends Cogn. Sci. 9 (10), 474–480. ISSN 1364-6613. https://do

i.org/10.1016/j.tics.2005.08.011. http://www.sciencedirect.com/science/article/pii/S1364661305002421.
Gans, F., Schumann, A.Y., Kantelhardt, J.W., Penzel, T., Fietze, I., Mar 2009. Cross-modulated amplitudes and frequencies characterize interacting components in complex systems. Phys. Rev. Lett. 102, 098701 https://doi.org/10.1103/PhysRevLett.102.098701. https://link.aps.org/doi/10.1103/PhysRevLett.102.098701.
Gerber, E.M., Sadeh, B., Ward, A., Knight, R.T., Deouell, L.Y., 2016. Non-sinusoidal activity can produce cross-frequency coupling in cortical signals in the absence of functional interaction between neural sources. PLoS One 11 (12), 1–19. https://doi.org/10.1371/journal.pone.0167351, 12. https://doi.org/10.1371/journal.pone.0167351.
Guckenheimer, J.M., Holmes, P., 2002. Nonlinear Oscillations, Dynamical Systems, and Bifurcations of Vector Fields. Springer.
Gunduz, A., Morita, H., Rossi, P.J., Allen, W.L., Alterman, R.L., Bronte-Stewart, H., Butson, C.R., Charles, D., Deckers, S., de Hemptinne, C., DeLong, M., Dougherty, D., Ellrich, J., Foote, K.D., Giordano, J., Goodman, W., Greenberg, B.D., Greene, D., Gross, R., Judy, J.W., Karst, E., Kent, A., Kopell, B., Lang, A., Lozano, A., Lungu, C., Lyons, K.E., Machado, A., Martens, H., McIntyre, C., Min, H.-K., Neimat, J., Ostrem, J., Pannu, S., Ponce, F., Pouratian, N., Reymers, D., Schrock, L., Sheth, S., Shih, L., Stanslaski, S., Steinke, G.K., Stypulkowski, P., Trster, A.I., Verhagen, L., Walker, H., Okun, M.S., 2015. Proceedings of the second annual deep brain stimulation think tank: what's in the pipeline. Int. J. Neurosci. 125 (7), 475–485. https://doi.org/10.3109/00207454.2014.999268. https://doi.org/10.3109/00207454.2014.999268. PMID: 25526555.
Hathaway, D.H., Mar 2010. The solar cycle. Living Rev. Sol. Phys. 7 (1), 1. https://doi.org/10.12942/lrsp-2010-1. ISSN 1614-4961. https://doi.org/10.12942/lrsp-2010-1.
He, B.J., Zempel, J.M., Snyder, A.Z., Raichle, M.E., May 2010. The temporal structures and functional significance of scale-free brain activity. Neuron 66 (3), 353–369.
Helfrich, R.F., Huang, M., Wilson, G., Knight, R.T., 2017. Prefrontal cortex modulates posterior alpha oscillations during top-down guided visual perception. Proc. Natl. Acad. Sci. 114 (35), 9457–9462. https://doi.org/10.1073/pnas.1705965114. ISSN 0027-8424. https://www.pnas.org/content/114/35/9457.
Helfrich, R.F., Mander, B.A., Jagust, W.J., Knight, R.T., Walker, M.P., Jan 2018. Old brains come uncoupled in sleep: slow wave-spindle synchrony, brain atrophy, and forgetting. Neuron 97 (1), 221–230.
Hoermann, R., Midgley, J.E.M., Larisch, R., Dietrich, J.W., 2015. Homeostatic control of the thyroidpituitary axis: perspectives for diagnosis and treatment. Front. Endocrinol. 6, 177. https://doi.org/10.3389/fendo.2015.00177. ISSN 1664-2392. https://www.frontiersin.org/article/10.3389/fendo.2015.00177.
Huelsemann, M.J., Naumann, E., Rasch, B., 2018. Quantification of Phase-Amplitude Coupling in Neuronal Oscillations: Comparison of Phase-Locking Value, Mean Vector Length, and Modulation Index. bioRxiv. https://doi.org/10.1101/290361. https://www.biorxiv.org/content/early/2018/03/28/290361.
Hyafil, A., 2015. Misidentifications of specific forms of cross-frequency coupling: three warnings. Front. Neurosci. 9, 370. https://doi.org/10.3389/fnins.2015.00370. ISSN 1662-453X. https://www.frontiersin.org/article/10.3389/fnins.2015.00370.
Hyafil, A., Fontolan, L., Kabdebon, C., Gutkin, B., Giraud, A.-L., 2015a. Speech encoding by coupled cortical theta and gamma oscillations. eLife 4, e06213. https://doi.org/10.7554/eLife.06213. ISSN 2050-084X. https://doi.org/10.7554/eLife.06213.
Hyafil, A., Giraud, A.-L., Fontolan, L., Gutkin, B., 2015b. Neural cross-frequency coupling: connecting architectures, mechanisms, and functions. Trends Neurosci. 38 (11), 725–740. ISSN 0166-2236. https://doi.org/10.1016/j.tins.2015.09.001. http://www.sciencedirect.com/science/article/pii/S0166223615002088.
Ieva, A.D., Schmitz, E.M., Cusimano, M.D., 2013. Analysis of intracranial pressure: past, present, and future. The Neuroscientist 19 (6), 592–603. https://doi.org/10.1177/1073858412474845. https://doi.org/10.1177/1073858412474845. PMID: 23389057.
Izhikevich, E.M., 2014. Dynamical Systems in Neuroscience: the Geometry of Excitability and Bursting. MIT Press.
Jensen, O., Colgin, L.L., 2007. Cross-frequency coupling between neuronal oscillations. Trends Cogn. Sci. 11 (7), 267–269. ISSN 1364-6613. https://doi.org/10.1016/j.tics.2007.05.003. http://www.sciencedirect.com/science/article/pii/S1364661307001271.
Jensen, O., Mazaheri, A., 2010. Shaping functional architecture by oscillatory alpha activity: gating by inhibition. Front. Hum. Neurosci. 4, 186. https://doi.org/10.3389/fnhum.2010.00186. ISSN 1662-5161. https://www.frontiersin.org/article/10.3389/fnhum.2010.00186.
Jensen, O., Spaak, E., Park, H., 2016. Discriminating valid from spurious indices of phase-amplitude coupling. eNeuro 3 (6). https://doi.org/10.1523/ENEURO.0334-16.2016. http://www.eneuro.org/content/3/6/ENEURO.0334-16.2016.
Jones, S.R., 2016. When brain rhythms aren't rhythmic: implication for their mechanisms and meaning. Curr. Opin. Neurobiol. 40, 72–80. ISSN 0959-4388. https://doi.org/10.1016/j.conb.2016.06.010. http://www.sciencedirect.com/science/article/pii/S0959438816300769. Systems neuroscience.
Kramer, M.A., Roopun, A.K., Carracedo, L.M., Traub, R.D., Whittington, M.A., Kopell, N.J., 2008a. Rhythm generation through period concatenation in rat somatosensory cortex. PLoS Comput. Biol. 4 (9), 1–16. https://doi.org/10.1371/journal.pcbi.1000169, 09. https://doi.org/10.1371/journal.pcbi.1000169.
Kramer, M.A., Tort, A.B., Kopell, N.J., 2008b. Sharp edge artifacts and spurious coupling in eeg frequency comodulation measures. J. Neurosci. Methods 170 (2), 352–357. ISSN 0165-0270. https://doi.org/10.1016/j.jneumeth.2008.01.020. http://www.sciencedirect.com/science/article/pii/S0165027008000538.
Krupa, M., Vidal, A., Desroches, M., Clément, F., Feb 2012. Mixed-mode Oscillations in a Multiple Time Scale Phantom Bursting System. 1202.2705.
Kullback, S., Leibler, R.A., 1951. On information and sufficiency. Ann. Math. Stat. 22 (1), 79–86. https://doi.org/10.1214/aoms/1177729694, 03. https://doi.org/10.1214/aoms/1177729694.
Kuznetsov, Y.A., 1998. Elements of Applied Bifurcation Theory. Springer.
Lakatos, P., Shah, A.S., Knuth, K.H., Ulbert, I., Karmos, G., Schroeder, C.E., 2005. An oscillatory hierarchy controlling neuronal excitability and stimulus processing in the auditory cortex. J. Neurophysiol. 94 (3), 1904–1911. https://doi.org/10.1152/jn.00263.2005. https://doi.org/10.1152/jn.00263.2005. PMID: 15901760.
Lakatos, P., Karmos, G., Mehta, A.D., Ulbert, I., Schroeder, C.E., 2008. Entrainment of neuronal oscillations as a mechanism of attentional selection. Science 320 (5872), 110–113. https://doi.org/10.1126/science.1154735. ISSN 0036-8075. http://science.sciencemag.org/content/320/5872/110.
Lanciego, J.L., Luquin, N., Obeso, J.A., 2012. Functional neuroanatomy of the basal ganglia. Cold Spring Harbor Perspectives in Medicine 2 (12). https://doi.org/10.1101/cshperspect.a009621. http://perspectivesinmedicine.cshlp.org/content/2/12/a009621.abstract.
Laskar, F.I., Pallamraju, D., Veenadhari, B., Aug 2014. Vertical coupling of atmospheres: dependence on strength of sudden stratospheric warming and solar activity. Earth Planets Space 66 (1), 94. https://doi.org/10.1186/1880-5981-66-94. ISSN 1880-5981. https://doi.org/10.1186/1880-5981-66-94.
Leblois, A., Boraud, T., Meissner, W., Bergman, H., Hansel, D., 2006. Competition between feedback loops underlies normal and pathological dynamics in the basal ganglia. J. Neurosci. 26 (13), 3567–3583. https://doi.org/10.1523/JNEUROSCI.5050-05.2006. ISSN 0270-6474. http://www.jneurosci.org/content/26/13/3567.
Lisman, J.E., Jensen, O., Mar 2013. The Theta - gamma neural code. Neuron 77 (6), 1002–1016.
López-Azcárate, J., Tainta, M., Rodríguez-Oroz, M.C., Valencia, M., González, R., Guridi, J., Iriarte, J., Obeso, J.A., Artieda, J., Alegre, M., 2010. Coupling between beta and high-frequency activity in the human subthalamic nucleus may be a pathophysiological mechanism in Parkinson's disease. J. Neurosci. 30 (19), 6667–6677. https://doi.org/10.1523/JNEUROSCI.5459-09.2010. ISSN 0270-6474. http://www.jneurosci.org/content/30/19/6667.
Lozano-Soldevilla, D., ter Huurne, N., Oostenveld, R., 2016. Neuronal oscillations with non-sinusoidal morphology produce spurious phase-to-amplitude coupling and directionality. Front. Comput. Neurosci. 10, 87. https://doi.org/10.3389/fncom.2016.00087. ISSN 1662-5188. https://www.frontiersin.org/article/10.3389/fncom.2016.00087.
Mazzoni, A., Panzeri, S., Logothetis, N.K., Brunel, N., 2008. Encoding of naturalistic stimuli by local field potential spectra in networks of excitatory and inhibitory neurons. PLoS Comput. Biol. 4 (12), 1–20. https://doi.org/10.1371/journal.pcbi.1000239, 12. https://doi.org/10.1371/journal.pcbi.1000239.
Mitry, J., McCarthy, M., Kopell, N., Wechselberger, M., Aug 2013. Excitable neurons, firing threshold manifolds and canards. J. Math. Neurosci. 3 (1), 12.
Mukamel, E.A., Pirondini, E., Babadi, B., Wong, K.F.K., Pierce, E.T., Harrell, P.G., Walsh, J.L., Salazar-Gomez, A.F., Cash, S.S., Eskandar, E.N., Weiner, V.S., Brown, E.N., Purdon, P.L., 2014. A transition in brain state during propofol-induced unconsciousness. J. Neurosci. 34 (3), 839–845. https://doi.org/10.1523/JNEUROSCI.5813-12.2014. ISSN 0270-6474. http://www.jneurosci.org/content/34/3/839.
Nambu, A., Tokuno, H., Takada, M., Jun 2002. Functional significance of the cortico-subthalamo-pallidal 'hyperdirect' pathway. Neurosci. Res. 43 (2), 111–117.
Onslow, A.C., Bogacz, R., Jones, M.W., 2011. Quantifying phaseamplitude coupling in neuronal network oscillations. Prog. Biophys. Mol. Biol. 105 (1), 49–57. ISSN 0079-6107. https://doi.org/10.1016/j.pbiomolbio.2010.09.007. http://www.sciencedirect.com/science/article/pii/S0079610710000751. BrainModes: The role of neuronal oscillations in health and disease).
Onslow, A.C.E., Jones, M.W., Bogacz, R., 2014. A canonical circuit for generating phase-amplitude coupling. PLoS One 9 (8), 1–15. https://doi.org/10.1371/journal.pone.0102591, 08. https://doi.org/10.1371/journal.pone.0102591.
Paluš, M., Feb 2014. Multiscale atmospheric dynamics: cross-frequency phase-amplitude coupling in the air temperature. Phys. Rev. Lett. 112 https://doi.org/10.1103/PhysRevLett.112.078702, 078702. https://link.aps.org/doi/10.1103/PhysRevLett.112.078702.
Palva, J.M., Palva, S., Kaila, K., 2005. Phase synchrony among neuronal oscillations in the human cortex. J. Neurosci. 25 (15), 3962–3972. https://doi.org/10.1523/JNEUROSCI.4250-04.2005. ISSN 0270-6474. http://www.jneurosci.org/content/25/15/3962.
Penny, W., Duzel, E., Miller, K., Ojemann, J., 2008. Testing for nested oscillation. J. Neurosci. Methods 174 (1), 50–61. ISSN 0165-0270. https://doi.org/10.1016/j.jneumeth.2008.06.035. http://www.sciencedirect.com/science/article/pii/S0165027008003816.
Purdon, P.L., Pierce, E.T., Mukamel, E.A., Prerau, M.J., Walsh, J.L., Wong, K.F.K., Salazar-Gomez, A.F., Harrell, P.G., Sampson, A.L., Cimenser, A., Ching, S., Kopell, N.J., Tavares-Stoeckel, C., Habeeb, K., Merhar, R., Brown, E.N., 2013. Electroencephalogram signatures of loss and recovery of consciousness from propofol. Proc. Natl. Acad. Sci. 110 (12), E1142–E1151. https://doi.org/10.1073/pnas.1221180110. ISSN 0027-8424. https://www.pnas.org/content/110/12/E1142.
Ray, S., Maunsell, J.H., Sep 2010. Differences in gamma frequencies across visual cortex restrict their possible use in computation. Neuron 67 (5), 885–896.
Richardson, A.G., Liu, X., Weigand, P.K., Hudgins, E.D., Stein, J.M., Das, S.R., Proekt, A., Kelz, M.B., Zhang, M., Van der Spiegel, J., Lucas, T.H., 2017. Hippocampal gamma-slow oscillation coupling in macaques during sedation and sleep. Hippocampus 27

(11), 1125–1139. https://doi.org/10.1002/hipo.22757. https://onlinelibrary.wiley.com/doi/abs/10.1002/hipo.22757.
Sanders, T.H., Devergnas, A., Wichmann, T., Clements, M.A., Nov 2013. Canonical correlation to estimate the degree of parkinsonism from local field potential and electroencephalographic signals. In: 2013 6th International IEEE/EMBS Conference on Neural Engineering (NER), pp. 158–161. https://doi.org/10.1109/NER.2013.6695896.
Sase, T., Katori, Y., Komuro, M., Aihara, K., 2017. Bifurcation analysis on phase-amplitude cross-frequency coupling in neural networks with dynamic synapses. Front. Comput. Neurosci. 11 (18) https://doi.org/10.3389/fncom.2017.00018. ISSN 1662-5188. https://www.frontiersin.org/article/10.3389/fncom.2017.00018.
Scheffer-Teixeira, R., Belchior, H., Caixeta, F.V., Souza, B.C., Ribeiro, S., Tort, A.B., Oct 2012. Theta phase modulates multiple layer-specific oscillations in the CA1 region. Cerebr. Cortex 22 (10), 2404–2414.
Schevon, C.A., Weiss, S.A., Emerson, R.G., Banks, G.P., McKhann, J., Guy, M., Goodman, R.R., Trevelyan, A.J., 2013. Ictal high frequency oscillations distinguish two types of seizure territories in humans, 10 Brain 136 (12), 3796–3808. https://doi.org/10.1093/brain/awt276. ISSN 0006-8950. https://dx.doi.org/10.1093/brain/awt276.
Schroll, H., Hamker, F., 2013. Computational models of basal-ganglia pathway functions: focus on functional neuroanatomy. Front. Syst. Neurosci. 7 (122) https://doi.org/10.3389/fnsys.2013.00122. ISSN 1662-5137. https://www.frontiersin.org/article/10.3389/fnsys.2013.00122.
Shapoval, A., Le Moul, J.-L., Shnirman, M., Courtillot, V., 2017. Dynamics of sunspot series on time scales from days to years: correlation of sunspot births, variable lifetimes, and evolution of the high-frequency spectral component. J. Geophys. Res.: Space Physics 122 (12). https://doi.org/10.1002/2017JA024430, 11,874–11,887. https://agupubs.onlinelibrary.wiley.com/doi/abs/10.1002/2017JA024430.
Shimamoto, S.A., Ryapolova-Webb, E.S., Ostrem, J.L., Galifianakis, N.B., Miller, K.J., Starr, P.A., 2013. Subthalamic nucleus neurons are synchronized to primary motor cortex local field potentials in Parkinson's disease. J. Neurosci. 33 (17), 7220–7233. https://doi.org/10.1523/JNEUROSCI.4676-12.2013. ISSN 0270-6474. http://www.jneurosci.org/content/33/17/7220.
Shriki, O., Hansel, D., Sompolinsky, H., 2003. Rate models for conductance-based cortical neuronal networks. Neural Comput. 15 (8), 1809–1841. https://doi.org/10.1162/08997660360675053. https://doi.org/10.1162/08997660360675053.
Soplata, A.E., McCarthy, M.M., Sherfey, J., Lee, S., Purdon, P.L., Brown, E.N., Kopell, N., 2017. Thalamocortical control of propofol phase-amplitude coupling. PLoS Comput. Biol. 13 (12), 1–24. https://doi.org/10.1371/journal.pcbi.1005879, 12. https://doi.org/10.1371/journal.pcbi.1005879.
Sotero, R.C., 2016. Topology, cross-frequency, and same-frequency band interactions shape the generation of phase-amplitude coupling in a neural mass model of a cortical column. PLoS Comput. Biol. 12 (11), 1–29. https://doi.org/10.1371/journal.pcbi.1005180, 11. https://doi.org/10.1371/journal.pcbi.1005180.
Swenson, R., 2006. Review of Clinical and Functional Neuroscience. Chapter 8 - Motor Systems. https://www.dartmouth.edu/~rswenson/NeuroSci/chapter_8.html.
Takeuchi, S., Mima, T., Murai, R., Shimazu, H., Isomura, Y., Tsujimoto, T., 2015. Gamma oscillations and their cross-frequency coupling in the primate Hippocampus during sleep, 07 Sleep 38 (7), 1085–1091. https://doi.org/10.5665/sleep.4818. ISSN 0161-8105. https://dx.doi.org/10.5665/sleep.4818.
Tort, A.B.L., Kramer, M.A., Thorn, C., Gibson, D.J., Kubota, Y., Graybiel, A.M., Kopell, N.J., 2008. Dynamic cross-frequency couplings of local field potential oscillations in rat striatum and hippocampus during performance of a t-maze task. Proc. Natl. Acad. Sci. 105 (51), 20517–20522. https://doi.org/10.1073/pnas.0810524105. ISSN 0027-8424. https://www.pnas.org/content/105/51/20517.
Tort, A.B.L., Komorowski, R.W., Manns, J.R., Kopell, N.J., Eichenbaum, H., 2009. Theta–gamma coupling increases during the learning of item–context associations. Proc. Natl. Acad. Sci. 106 (49), 20942–20947. https://doi.org/10.1073/pnas.0911331106. ISSN 0027-8424. https://www.pnas.org/content/106/49/20942.
Tort, A.B.L., Komorowski, R., Eichenbaum, H., Kopell, N., 2010. Measuring phase-amplitude coupling between neuronal oscillations of different frequencies. J. Neurophysiol. 104 (2), 1195–1210. https://doi.org/10.1152/jn.00106.2010. https://doi.org/10.1152/jn.00106.2010. PMID: 20463205.
Tsiokos, C., Malekmohammadi, M., AuYong, N., Pouratian, N., 2017. Pallidal low beta-low gamma phase-amplitude coupling inversely correlates with Parkinson disease symptoms. Clin. Neurophysiol. 128 (11), 2165–2178. ISSN 1388-2457. https://doi.org/10.1016/j.clinph.2017.08.001. http://www.sciencedirect.com/science/article/pii/S1388245717309185.
van Driel, J., Cox, R., Cohen, M.X., 2015. Phase-clustering bias in phaseamplitude cross-frequency coupling and its removal. J. Neurosci. Methods 254, 60–72. ISSN 0165-0270. https://doi.org/10.1016/j.jneumeth.2015.07.014. http://www.sciencedirect.com/science/article/pii/S016502701500268X.
van Wijk, B.C., Beudel, M., Jha, A., Oswal, A., Foltynie, T., Hariz, M.I., Limousin, P., Zrinzo, L., Aziz, T.Z., Green, A.L., Brown, P., Litvak, V., 2016. Subthalamic nucleus phaseamplitude coupling correlates with motor impairment in Parkinsons disease. Clin. Neurophysiol. 127 (4), 2010–2019. ISSN 1388-2457. https://doi.org/10.1016/j.clinph.2016.01.015. http://www.sciencedirect.com/science/article/pii/S1388245716000468.
Vaz, A.P., Yaffe, R.B., Wittig, J.H., Inati, S.K., Zaghloul, K.A., 2017. Dual origins of measured phase-amplitude coupling reveal distinct neural mechanisms underlying episodic memory in the human cortex. Neuroimage 148, 148–159. ISSN 1053-8119. https://doi.org/10.1016/j.neuroimage.2017.01.001. http://www.sciencedirect.com/science/article/pii/S1053811917300010.
Velarde, O.M., Mato, G., Dellavale, D., 2017. Mechanisms for pattern specificity of deep-brain stimulation in Parkinsons disease. PLoS One 12 (8), 1–30. https://doi.org/10.1371/journal.pone.0182884, 08. https://doi.org/10.1371/journal.pone.0182884.
Voytek, B., Canolty, R., Shestyuk, A., Crone, N., Parvizi, J., Knight, R., 2010. Shifts in gamma phaseamplitude coupling frequency from theta to alpha over posterior cortex during visual tasks. Front. Hum. Neurosci. 4, 191. https://doi.org/10.3389/fnhum.2010.00191. ISSN 1662-5161. https://www.frontiersin.org/article/10.3389/fnhum.2010.00191.
West, T.O., Berthouze, L., Halliday, D.M., Litvak, V., Sharott, A., Magill, P.J., Farmer, S.F., 2018. Propagation of beta/gamma rhythms in the cortico-basal ganglia circuits of the parkinsonian rat. J. Neurophysiol. 119 (5), 1608–1628. https://doi.org/10.1152/jn.00629.2017. https://doi.org/10.1152/jn.00629.2017. PMID: 29357448.
White, J.A., Banks, M.I., Pearce, R.A., Kopell, N.J., 2000. Networks of interneurons with fast and slow gamma-aminobutyric acid type a (gabaa) kinetics provide substrate for mixed gamma-theta rhythm. Proc. Natl. Acad. Sci. 97 (14), 8128–8133. https://doi.org/10.1073/pnas.100124097. ISSN 0027-8424. https://www.pnas.org/content/97/14/8128.
Wilson, H.R., Cowan, J.D., Jan 1972. Excitatory and inhibitory interactions in localized populations of model neurons. Biophys. J. 12 (1), 1–24.
Wulff, P., Ponomarenko, A.A., Bartos, M., Korotkova, T.M., Fuchs, E.C., Bähner, F., Both, M., Tort, A.B.L., Kopell, N.J., Wisden, W., Monyer, H., 2009. Hippocampal theta rhythm and its coupling with gamma oscillations require fast inhibition onto parvalbumin-positive interneurons. Proc. Natl. Acad. Sci. 106 (9), 3561–3566. https://doi.org/10.1073/pnas.0813176106. ISSN 0027-8424. https://www.pnas.org/content/106/9/3561.
Yang, Y., Lin, C., 2005. Vehicle-bridge interaction dynamics and potential applications. J. Sound Vib. 284 (1), 205–226. ISSN 0022-460X. https://doi.org/10.1016/j.jsv.2004.06.032. http://www.sciencedirect.com/science/article/pii/S0022460X04005863.